UNIVERSITY OF BIRMINGHAM

University of Birmingham
Research at Birmingham

Flow, turbulence and potential droplet break up mechanisms in an in-line Silverson 150/250 high shear mixer

Espinoza, C.J.U.; Alberini, F.; Mihailova, O.; Kowalski, A.J.; Simmons, M.J.H.

[Link to publication on Research at Birmingham portal](#)

Flow, turbulence and potential droplet break up mechanisms in an in-line Silverson 150/250 high shear mixer

C.J.U. Espinoza [a,b], F. Alberini [a], O. Mihailova [b], A.J. Kowalski [b], M.J.H. Simmons [a,*]

[a] School of Chemical Engineering, University of Birmingham, Edgbaston, Birmingham B15 2TT, UK
[b] Unilever R&D, Port Sunlight Laboratory, Bebington, Wirral CH63 3JW, UK

ABSTRACT

Angle resolved 2-D PIV measurements were performed to characterise the flow and turbulence as well as indicate potential droplet break up mechanisms in an in-line Silverson 150/250 high shear mixer, using water as the working fluid in the turbulent regime ($120,000 < Re < 420,000$). Distributions of Reynolds stresses, turbulent kinetic energy (TKE), and energy dissipation rates (ε) were examined. The regions of interest (ROI) were: A – jet emanating from a stator hole and B – the rotor swept volume. The complex flow pattern can cause droplet break up under either laminar or turbulent conditions depending on the characteristic length and velocity in the ROI; break up due to turbulence in the inertial regime was identified as the dominant mechanism in this study. Evaluated energy dissipation rates obtained assuming either a fully resolved velocity field (DE) or using the Smagorinsky closure model (SGS) were found to depend on rotor speed e.g. $\varepsilon \propto N^b$ with b exponents of 1.59–1.90 (DE) and 2.42–2.84 (SGS), which are comparable to existing literature values. The influence on ε of the rotor speed, external pump flow rate and induced backpressure on the mixer outlet, were also investigated. Analysis revealed that the intensity and propensity of ε is dictated by the dominant flow in the mixing head e.g. radial flow at high pump flow rates, prominent in ROI A or tangential flow at high rotor speeds and when backpressure is induced, prominent in ROI B.

© 2020 The Authors. Published by Elsevier Ltd. This is an open access article under the CC BY license (http://creativecommons.org/licenses/by/4.0/).

1. Introduction

'Rotor-stator' Mixers (RSM), or high shear mixers (HSM), are extensively used in industrial processes for liquid-liquid dispersion, emulsification and homogenisation due to their capability to produce high levels of shear and energy dissipation rates (three orders of magnitude greater than a mechanically stirred vessel) on a relatively small volume of fluid. They are used in the food, cosmetics, home and personal care as well as pharmaceutical industries for manufacturing products such as mayonnaise, detergents, shampoos and conditioners (Håkansson, 2018; Zhang et al., 2012) and can be operated in batch, semi-continuous or continuous (in-line) modes. They may also be classified as axial and radial discharge HSMs, toothed devices and colloid mills and they are manufactured by companies such as Ross, Chemineer, IKA work, Siefer, Rayneri and Silverson with a range of scales and geometries to suit a given application (Utomo, 2009).

HSM mixing heads consist of a high speed rotor (rotating mixing element with a typical tip speed range of 10–50 m s^{-1}) and a stator (fixed mixing element) which are in close proximity to each other (Atiemo-Obeng and Calabrese, 2004), with a rotor-stator (R-S) gap ranging from 100 to 3000 μm (Karbstein and Schubert, 1995). The operating principle involves drawing the fluid axially into the R-S gap; exposing it to high tangential velocity gradients and turbulence (equivalent shear rates from 20,000 to 100,000 s^{-1}); and eventually ejecting it radially in the form of jets through the stator holes (Utomo et al., 2009; Zhang et al., 2012).

Despite the abundance of these devices, publications detailing aspects of their design and basis of operation have only surfaced over the last decade and therefore previous optimisation of operating parameters has been heavily reliant on operator experience and trial-and-error (Mortensen et al., 2017). Literature on both batch and in-line HSMs has focussed on the development of scaling rules and features of the turbulence within the mixing head. The majority of studies have either been purely experimental, focussing on droplet break-up (Carrillo De Hert and Rodgers, 2017; Hall, 2012; Hall et al., 2011; James et al., 2017a; Rodgers and Cooke, 2012; Rueger and Calabrese, 2013a; b; Shi et al., 2013; Thapar, 2004), measurement of power consumption (Cooke et al., 2012; James et al., 2017b; Kowalski et al., 2011; Padron, 2001; Sparks, 1993; Xu et al., 2013b), or flow visualisation studies using

Nomenclature

Symbols

B	rotor blade width, m
C_S	Smagorinsky constant, dimensionless
D	filled volume diameter, m
D_h	stator hole diameter, m
D_{inlet}	inlet pipe diameter, m
$D_{ps,\,inner}$	primary stator inner diameter, m
$D_{ps,\,outer}$	primary stator outer diameter, m
$D_{r,i}$	inner rotor diameter, m
$D_{r,o}$	outer rotor diameter, m
$D_{ss,\,inner}$	secondary stator inner diameter, m
$D_{ss,\,outer}$	secondary stator outer diameter, m
D_{volute}	hydraulic diameter between $D_{ss,\,outer}$ and filled volume diameter (2R), m
k	turbulent kinetic energy, $m^2\,s^{-2}$
k_1	proportionality constant in Eq. (5), dimensionless
L	turbulent (integral) length scale, m
L_{IA}	side length of interrogation area, m
L_p	side length of interrogation area, pixels
M_P	external pump mass flow rate, $kg\,s^{-1}$
M_S	generated mass flow rate by Silverson, $kg\,s^{-1}$
M_T	total mass flow rate, $kg\,s^{-1}$
N	rotor speed, rps
P	power constant, W
P_{OUT}	outlet pressure, bar
Po_Z	'zero flow' power constant in Eq. (5), dimensionless
Q	volumetric flow rate, $m^3\,s^{-1}$
R_{11}	normal Reynolds stresses in the x-direction, $m^2\,s^{-2}$
R_{12}	shear Reynolds stresses in the xy-plane, $m^2\,s^{-2}$
R_{22}	normal Reynolds stresses in the y-direction, $m^2\,s^{-2}$
Re	impeller Reynolds number, dimensionless
Re_T	turbulence Reynolds number $\left(\frac{k^2}{\varepsilon v}\right)$, dimensionless
S	magnification, dimensionless
S_r	row separation distance, m
U	mean velocity, $m\,s^{-1}$
$\overline{U}\vert_\theta$	angle resolved mean velocity, $m\,s^{-1}$
U_p	periodic velocity component of the flow, $m\,s^{-1}$
U	instantaneous velocity, $m\,s^{-1}$
U_f	fluctuating velocity component, $m\,s^{-1}$
U_{hole}	stator hole velocity, $m\,s^{-1}$
U_{inlet}	inlet pipe velocity, $m\,s^{-1}$
U_{jet}	jet velocity, $m\,s^{-1}$
U_{max}	maximum velocity, $m\,s^{-1}$
U_{rms}	root mean square (RMS) of the fluctuating velocity, $m\,s^{-1}$
U_{tip}	rotor tip speed (πND), $m\,s^{-1}$
U_x	x-component of velocity in Cartesian coordinates, $m\,s^{-1}$
U_y	y-component of velocity in Cartesian coordinates, $m\,s^{-1}$
V	volume in Eq. (4), m^3
V_δ	rotor-stator gap volume, m^3
V_{hole}	stator hole volume, m^3
V_{inlet}	entrance pipe volume, m^3
$V_{rotor\,swept}$	rotor swept volume, m^3
V_{volute}	volute volume, m^3
x, y, z	directions in Cartesian coordinates, m
z	arbitrary axial distance in cylindrical coordinates, m
Z	stator thickness, m

Greek letters

δ	Rotor-stator gap, m
Δ	grid spacing or filter width, m
ΔP	pressure drop, bar
ΔH	head, m
Δt	time delay between image pairs, s
ε	local specific energy dissipation rate, $m^2\,s^{-3}$
$\bar{\varepsilon}$	mean specific energy dissipation rate, $m^2\,s^{-3}$
ε_{avg}	power per unit mass, $W\,kg^{-1}$ ($m^2\,s^{-3}$)
λ_k	Kolmogorov length scale, m
μ	fluid viscosity, Pa s
ν	kinematic viscosity, $m^2\,s^{-1}$
ρ	fluid density, $kg\,m^{-3}$
τ_R	residence time, s

Dimensionless groups

$Re = \frac{\rho N D_{r,o}{}^2}{\mu}$ Reynolds number, dimensionless

Subscripts

A	in region A
B	in region B
c	continuous phase
d	dispersed phase
DE	by Direct Evaluation
P	pump
S	Silverson
SGS	using Smagorinsky sub-grid Scale
T	total

Superscripts'

'	fluctuating quantity from time-averaged data
''	fluctuating quantity from angle-resolved data
*	normalised values

Abbreviations

FOV	field of view
MHV	mixing head volume
PO	pump only
ROI	region of interest
RSV	rotor swept volume
SO	Silverson only
VFO	valve fully open
VPC	valve partially closed

techniques such as Laser Doppler Anemometry (LDA), Particle Image Velocimetry (PIV) and high speed imaging (Ashar et al., 2018; Espinoza et al., 2018; Håkansson et al., 2017a; Håkansson et al., 2017c; Mortensen et al., 2011; Mortensen et al., 2017; 2018; Sparks, 1996; Utomo et al., 2008) to study the effects of process parameters such as rotor (and pump for in-line devices) settings as well as the influence of stator designs. Some published work on numerical simulations have employed computational fluid dynamics (CFD) to characterise turbulence in several in-line HSM models (Ahmed et al., 2018; Håkansson et al., 2017b; Håkansson and Innings, 2017; Minnick et al., 2018; Utomo et al., 2009). Most recent work published in the literature focuses on validating CFD simulations via experiments (Jasińska et al., 2013; Jasińska et al., 2015; Kim, 2015; Qin et al., 2017; Utomo et al., 2008; Xu et al., 2013a; Zhang et al., 2017).

In spite of the above efforts and an increase in published articles on and around the topic, the number of studies remains relatively low compared to other well-established mixing equipment such as mechanically agitated vessels. This is because of the plethora of interacting factors that needs to be considered to fully characterise the fluid behaviour. These factors include, but are not limited to processing conditions such as flow rate and fluid properties, rotor and stator geometries as well as the mixing mechanisms involved and applications.

HSMs possess inherently complex flow patterns which results in an inhomogeneous distribution of energy in the mixing head. Thus, although HSMs usually operate in fully turbulent conditions e.g. including the bulk region, it means that flow at certain locations in the mixing head can be laminar, transitional or turbulent, depending on the characteristic velocity and length scale in the location of interest. Laminar flows such as simple shear and elongational flows may occur in the R-S gap and in the fluid through the stator holes (or at locations with varying cross-sections) respectively (Hall, 2012; Sparks, 1996; Thapar, 2004).

In turbulent flow, turbulent pressure fluctuations dominate the viscous stresses and are responsible for droplet break up. Mechanistic models developed by Hinze (1955) which assume homogeneous isotropic turbulence (at very high Reynolds numbers), are often used as theoretical basis. This crude assumption rarely applies in practical situations since the flow, especially in close proximity to the rotor, is intermittently anisotropic, yet it is often the only option available to the practising engineer (Ashar et al., 2018; Håkansson et al., 2017c; Hall et al., 2011; Thapar, 2004). Depending on whether the droplet size d, is larger or smaller than the Kolmogorov length scale, λ_K, the droplet break up mechanisms in the universal equilibrium range can be sub-divided into inertial and viscous- subranges where inertial and viscous forces dominate respectively. A competing theory by Rodgers and Cooke (2012) proposes that agitator shear rate causes break-up, based on a force balance between the interfacial forces and the external viscous stresses generated by the agitator. They suggest that the equilibrium droplet size correlates with the maximum shear rate and thus the rotor tip speed and argue that without the stator screen, a HSM is practically a very small stirred vessel. Empirical equations based upon the energy density $E_V = \left(\frac{P}{Q}\right)$, can also be used for droplet size correlations. This parameter ignores the effects of re-coalescence and encompasses the effects of process parameters applied to a particular volume of emulsion, which takes into consideration the mean residence time acting on the drop (Hall et al., 2011).

In industrial practice, an in-line mode of operation is more favourable due to the economic benefits in delivering larger continuous throughput (Qin et al., 2017). However, the lack of theoretical knowledge, even more than for batch operated HSMs, makes their design and application very challenging (Håkansson and Innings, 2017). Utomo et al. (2009) investigated the role of stator hole numbers, shapes and sizes and found that wider, far-spaced holes are more likely to develop stronger jets and recirculation which may be favourable for droplet break up. Espinoza et al. (2018) showed that the flow behaviour in an inline mixer equipped with an external pump was affected by the relative contribution of the mechanical energy inputted by both the mixing head and the pump, the former leading to a dominance of tangential flow and the latter leading to the creation of a strong radial flow component due to an increase of jetting through the stator holes. Additionally, Qin et al. (2017) found that having multiple rows of stator holes

also results in a complex flow pattern due to jet-to-jet interactions. Rodgers and Cooke (2012), together with Hall (2012), emphasised that the stator plays an essential role in reaching equilibrium droplet sizes faster in both single- and multi-pass emulsification. They also highlighted its importance at higher flow rates for droplet breakage where high velocities and pressure drop through the stator screens increase the shear through the holes. Moreover, Kowalski et al. (2011) highlighted that having multiple rows of small stator holes further increases the available surface area for shearing of the fluids. This is in line with the observations of Atiemo-Obeng and Calabrese (2004) that droplet break up occurs mainly from the stator walls and emanating jets from the stator holes due to the diversion and deceleration of the tangential flow imparted by the rotor (via the downstream face of the stator) to radial flow through the stator holes. The frequent and sudden acceleration (by the rotor) and deceleration (by the stator) is responsible for the main energy losses in the mixing head (Thapar, 2004). Finally, Håkansson et al. (2017c) and Ashar et al. (2018) further concluded that the probability of droplet break up due to collisions does not only depend on areas of intense turbulence but also on the local flow patterns which determine which areas are often visited by the drops.

The difference between the hydrodynamics of batch and in-line HSMs can influence droplet break up mechanisms (Håkansson et al., 2017b). Of the few studies on in-line HSMs, Sparks (1996) carried out flow visualisation experiments (through reactive mixing) and Thapar (2004) used these findings in combination with drop size analysis to determine the possible locations and potential mechanisms of droplet break up in turbulent flow, the results of which are summarised in Table 1. Furthermore, Thapar (2004) ordered these locations in terms of residence times: shear gap < stator < inlet pipe < rotor < volute, which indicates that small areas with high local energy dissipation rates are often bypassed by most drops and that most of them break by inertial and viscous stresses in the rotor region.

The complexity presented in the above literature confirms the current status quo that generic scale-up rules do not exist for either batch or inline HSMs and indeed Mortensen et al. (2011) stated that: "a general characterisation of rotor-stator mixer performance by simple mechanistic models does not seem realistic". The implication is that robust and validated CFD based models are a necessary tool for the practising engineer. Studies by Xu et al. (2013a), Xu et al. (2013b) and Zhang et al. (2017) investigated the hydrodynamics (LDA), power consumption (e.g. via torque measurements), residence time (pulse stimulus technique), strain and energy dissipation rate distributions (CFD) in a FLUKO® pilot-scale in-line HSM (model FDX1/60). However, these are single-phase experiments and thus no explicit links were made to emulsification processes. To date, performing visualisation experiments on emulsions (especially with PIV) is still very challenging or unachievable because of their inherent opacity. For techniques to work, emulsions have to be extremely dilute or

Table 1
Locations and proposed droplet breakup mechanisms under turbulent conditions in an in-line HSM (Sparks, 1996; Thapar, 2004).

Location	Breakup mechanism	Details
Inlet pipe	Inertial stresses	Inlet pipe flow is highly turbulent
Rotor region	Inertial and viscous stresses	Effective shear rates are very high; Re calculated indicative of turbulent condition; critical burst time ≪ residence time, deeming breakup due to viscous stress possible
Shear gap	Inertial subrange eddies when Re is high enough (although mainly viscous stress at lower Re)	Drops similar to or below $d_{3,2}$ will break in the short time spent in the gap
Stator	Viscous stresses (laminar only as Re relatively low)	Drops from shear gap will break further in this region
Volute	Inertial stresses	Volute flow is turbulent and is responsible to break larger drops that bypassed regions of high energy and shear rates

alternatively, independent visualisation and emulsification experiments, as done by Sparks (1996) and Thapar (2004) can be done. The latter evidently (Hall et al., 2011; Qin et al., 2017; Thapar, 2004) remains as the conventional and convenient choice as it is easier to analyse how droplet size distributions (DSD) and average drop sizes such as $d_{3,2}$ and $d_{4,3}$ of emulsion systems respond to changes in process parameters. More recently, collaborative work by Håkansson et al. (2017c) and Ashar et al. (2018) investigated where, when and how droplets break in a bespoke batch HSM using results from CFD simulations, PIV and visualisation of single droplet break up with particular attention to disruptive stresses. Their approach, using a variety of techniques, is compelling, yet, it is necessary to be aware of the limitations of the methods used (e.g. PIV resolution) in the interpretation of the data.

This paper presents a novel study of the hydrodynamics of a custom-built pilot-scale, Silverson 150/250 (double rotor, double stator) mixer equipped with an external pump for flow control. Measurements of the fluid motion were made using angle resolved 2-D PIV, with the aim of understanding how the flow is affected by process parameters, namely rotor speed, external pump flow rate and mixer backpressure. Determination of Reynolds stresses, turbulent kinetic energy (TKE) and energy dissipation rates from the PIV data, considering the resolution of the technique, is used to inform where in the mixing head droplet break up is most likely to occur (e.g. in areas of high energy dissipation) and to propose possible break up mechanisms.

2. Materials and methods

2.1. Equipment

The various equipment used in this study are identical to those used by Espinoza et al. (2018) and a schematic of the experimental rig is shown in Fig. 1. It consists of a 100 L vessel (1) fitted with a ball valve (2) at the outlet (DN25 PN25, NTC); a positive displacement pump (3) (DW1/007/7, SPX Flow); a Coriolis mass flow meter (4) (Optimass 7000C, Krohne) and a pilot scale in-line 150/250 MS Silverson rotor-stator mixer (5) (Silverson Machines Ltd) equipped with pressure (Cerebar M PMP51, Endress + Hauser Ltd) and temperature (PT100, Thermosense) sensors at the inlet and outlet as well as a proportional relief valve (6) (SS-RL4M8F8-SET, Swagelok). A needle valve (7) (SS-16GUF16, Swagelok) was used to control the backpressure at the mixer outlet. All units are connected with 1″ flexible braided pipes. A vortex breaker is also present at the bottom of the vessel (1) to prevent air entrainment.

The mixing head geometry is shown in Fig. 2 with the front view of the mixing head illustrated in Fig. 2a. All internal components including the double emulsor screens and double concentric rotors were made out of transparent polymethyl methacrylate to enable flow visualisation. The internal space within the head has a diameter $D = 108$ mm and the other dimensions illustrated in Fig. 2 are provided in Table 2. The rotor-stator gap is 0.23 mm and the stator height, Z is 15.875 mm. The thickness of the stators is ~2 mm.

2.2. Process conditions

Water was used as the working fluid and the measurements were performed in the turbulent regime over a range of Reynolds number, Re from 120,000–420,000, calculated using

$$Re = \frac{\rho N D_{r,o}^2}{\mu} \tag{1}$$

where ρ is the density, μ is the viscosity at a fixed temperature, N is the rotor speed and $D_{r,o}$ is the outer rotor diameter.

The pump was used to provide an externally driven flow rate, M_P in the mixing head (0.208–0.347 kg s^{-1}) and the rotor speed was controlled independently (30.0–103.3 rps); both were controlled using separate frequency inverters. The needle valve was also used to control the flow rate and backpressure in the mixing head, with the relief valve set at 5 bar (lower than the pressure rating of the mixing head of 7 bar). A data recorder (Memograph RSG45, Endress + Hauser) was used to log the mass flow rate, rotor speed, pressure and temperature at the mixer inlet and outlet. The flow meter was calibrated using the bucket and timer method and was found to be accurate within 1.3% in all experiments.

The parameters set for each experimental run are summarised in Table 3a. Runs 1–3 were carried out using the external pump only (PO), whereas runs 4 and 11 were carried out using the Silverson mixing head only with the pump switched off (SO). The remaining runs were carried out with both the pump and Silverson operating but with the outlet back pressure valve set either fully open (VFO), with mixer outlet pressure (P_{OUT}) ranging from 0.259 to 1.094 bar, or partially closed (VPC), P_{OUT} = 0.259–1.777 bar respectively. The total flow rate, M_T is the combined flow rates of the external pump (M_P) and the Silverson mixer (M_S). However, it is important to note that these are not additive e.g. $M_T \neq M_P + M_S$. For VPC conditions, the needle valve was partially closed after both the external pump and Silverson are in operation.

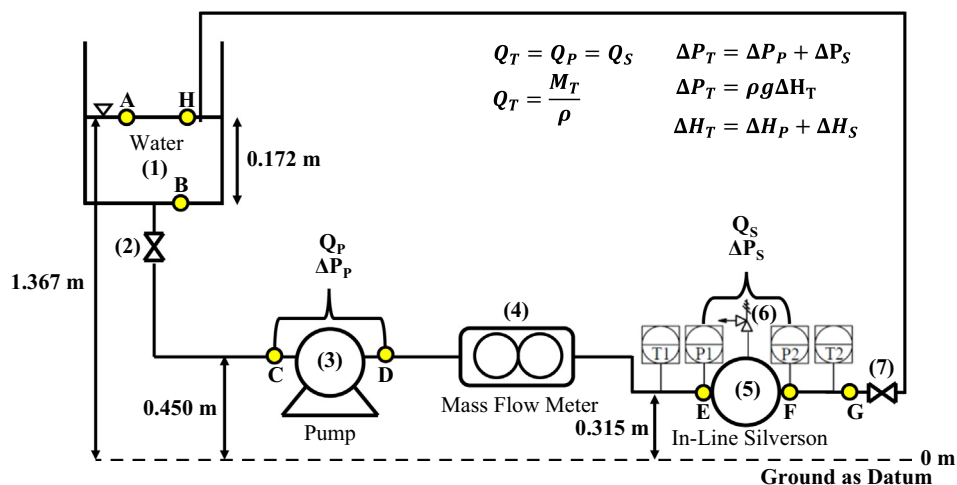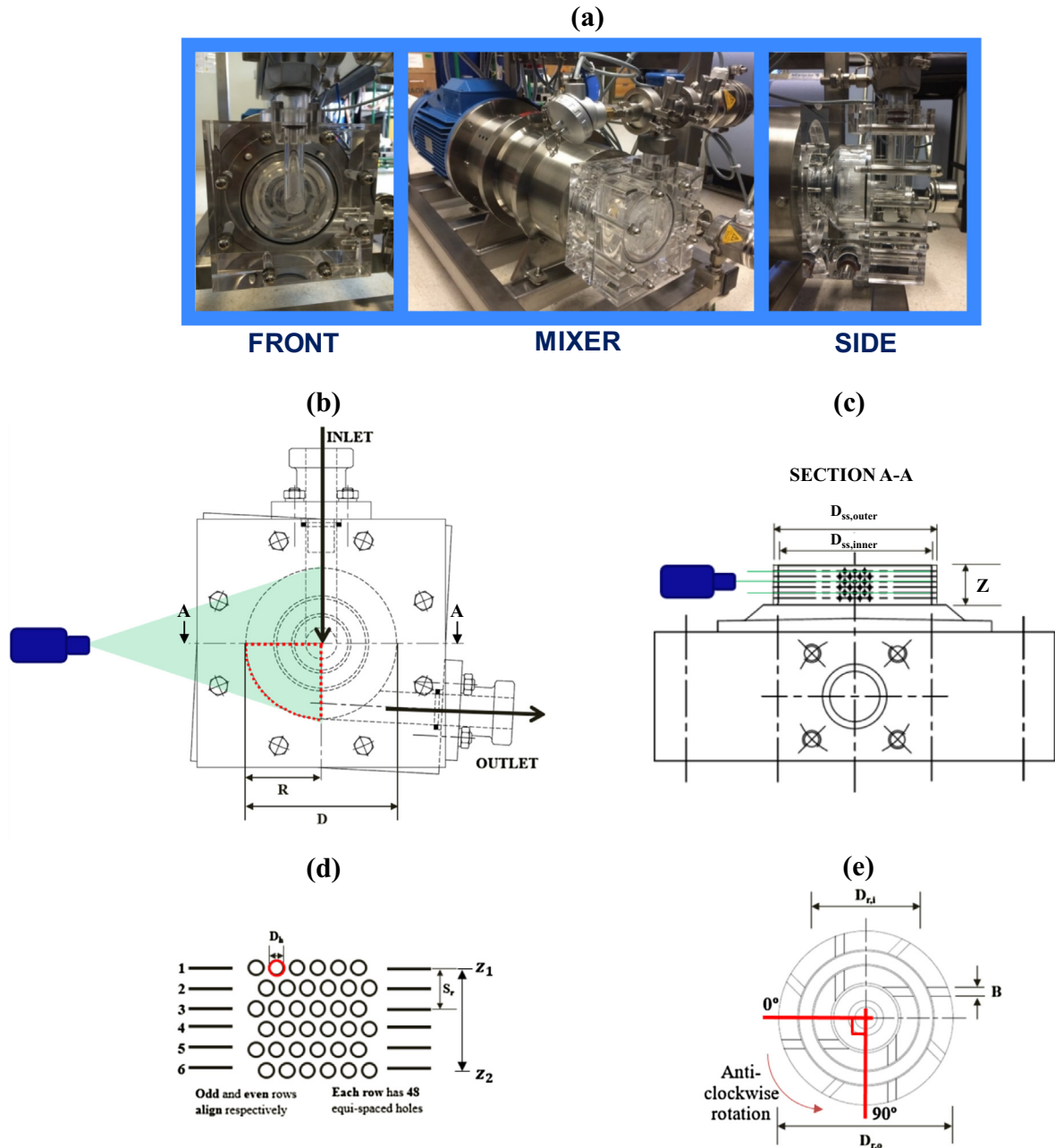

$$Q_T = Q_P = Q_S \qquad \Delta P_T = \Delta P_P + \Delta P_S$$
$$Q_T = \frac{M_T}{\rho} \qquad \Delta P_T = \rho g \Delta H_T$$
$$\Delta H_T = \Delta H_P + \Delta H_S$$

Fig. 1. Schematic of the experimental setup.

Fig. 2. (a) Photograph of the modified in-line Silverson 150/250 mixer (b) Mixing head inlet, outlet, laser sheet and region of interest at the front view (c) Section A-A: mixing head showing laser sheet positions from the top view (d) Secondary stator details (e) Rotors schematic at 0° position.

This is done to match the initially set flow rate, M_P before the Silverson was switched on (the pump is always switched on first). This enables the external pump to control the overall process flow rate and thus the fluid residence time in the mixer and also to prevent the Silverson from acting as a pump; and instead, focus on inputting energy and imposing shear on the fluid (Casugbo and Baker, 2018). This also throttles the Silverson's discharge which delays the onset of cavitation by reducing the net positive suction head (NPSH) required.

2.3. PIV experiments

The 2-D PIV measurements taken were angle resolved to the rotor position shown in Fig. 2d. The PIV system consists of a dual head 532 nm Nd-Yag laser (Litron Nano PIV) pulsing from 10 to 100 Hz, a 4 megapixel (2048 × 2048 pixels^2) single frame-straddling 12 bit CCD camera (630091, TSI Inc., USA), a synchroniser (610036, TSI Inc., USA) and a personal computer running TSI Insight 4G software. The outlet of the laser light arm and camera were mounted on a computer controlled traverse which has a precision of 0.2 mm. An optical tachometer is attached onto the mixer shaft to enable encoding of the rotor angle by sending a signal to the synchroniser at the 0° position. Other angles can then be set by inputting the necessary time delay into the Insight 4G software. The seeding particles used were silver coated hollow glass 10 μm diameter spheres with a density of 1400 kg m^{-3} (Dantec Inc., DK). They have been shown previously to have a short relaxation time and can be assumed to faithfully follow the fluid motion (Gabriele et al., 2009).

500 image pairs, and thus instantaneous velocity fields, were obtained for each experiment. It was demonstrated previously by Espinoza et al. (2018) that this is sufficient to ensure the turbulent

Table 2
Dimensions and details of the rotor–stator.

Item	Inner diameter (mm)	Outer diameter (mm)	Details
Inner rotor, $D_{r,i}$	38.10	–	4 blades Blade width, B = 3.17 mm
Outer rotor, $D_{r,o}$	63.50	–	8 blades Blade width, B = 3.17 mm
Primary stator (inner screen), D_{ps}	38.56	42.55	- 5 rows of 30 × D_h = 1.59 mm circular holes, 150 holes - Separation distance between aligned rows S_r = 4.75 mm
Secondary stator (outer screen), D_{ss}	63.96	68.33	- 6 rows of 48 × D_h = 1.59 mm circular holes, 288 holes - Separation distance between aligned rows S_r = 4.75 mm

features of the flow are captured. These data were used to calculate average velocity fields as well as Reynolds stresses, turbulent kinetic energy and energy dissipation rate. The images were processed using a recursive Nyquist grid algorithm using interrogation areas (IA) of 64 × 64 and 32 × 32 pixels for the first and second passes respectively. The Gaussian peak method by Westerweel (1997) was used to identify individual particles in the image.

The resolution of the PIV measurement depends upon the length scale of the IA, L_{IA}, which acts as a filter below which length scales are not resolved. Thus, there is a compromise between resolution and field of view (FOV). For the conducted experiments, the FOVs and spatial resolutions used are portrayed and summarised in Fig. 3 and Table 3a respectively. In these FOVs, two regions of interest (ROI): A (jet region) and B (high shear region) were studied (Fig. 3a). FOV 3 was used for the majority of the results obtained with a spatial resolution of 6.6 μm pixel⁻¹ which equates to a resolution of 210 μm for a 32 × 32 pixel IA, with vectors spaced 105 μm apart allowing for 50% overlap of IAs. The time delay between each image in an image pair was calculated in terms of the recommended maximum displacement travelled by a particle within an interrogation area, 0.25 L_{IA} (Adrian, 1986) using

$$\Delta t < \frac{0.25 L_{IA}}{U_{tip}} \qquad (2)$$

where $L_{IA} = S \times L_p$; where S is the magnification factor, L_p is the length of the IA in pixels and rotor tip speed, $U_{tip} = \pi N D$, and are summarised in Table 3a. In post-processing, velocities greater than U_{tip} as well as the vectors that failed the validation stage using the median test (5 × 5 neighbourhood size) were filtered out and replaced with interpolated values from the same grid size.

Despite numerous contributing factors to PIV data uncertainty, PIV system measurements have an accuracy of ~1–2% of the full-scale displacement range (Westerweel et al., 2013). The square outer section of the mixing head also ensured that reflections and optical distortions were minimised.

2.4. Analysis of PIV data

There is a compromise between the desired FOV and spatial resolution as the calculation of turbulence properties requires in principle full resolution of the flow field down to the Kolmogorov length scale, λ_k. This is challenging in terms of optics and seeding levels and would require multiple measurements to be taken of adjacent regions to adequately cover the area to be imaged, see for example (Khan et al., 2004). The method chosen in this work was to take three FOVs at different resolutions, a similar approach taken for dissipation rate studies in mechanically agitated vessels

Table 3a
Experimental runs and their corresponding power (calculated using Eq. (5)), power per unit mass (ε_{avg}), Kolmogorov length scales (λ_k) as well as the image acquisition parameters and spatial resolutions. *Calculated using. $P_{Pump} = (M_P/\rho)P_{in}$

Run (-)	Rotor speed, N (rps)	External pump flow rate, M_P (kg s⁻¹)	Flow class (-)	Measured total pump flow rate, M_T (kg s⁻¹)	P (kg m² s⁻³)	ε_{avg} (m² s⁻³)	λ_k (μm)	FOV 1 Δ (μm)	FOV 1 Δt (μs)	FOV 1 Δ/λ_k (-)	FOV 2 Δ (μm)	FOV 2 Δt (μs)	FOV 2 Δ/λ_k (-)	FOV 3 Δ (μm)	FOV 3 Δt (μs)	FOV 3 Δ/λ_k (-)
1	0.0	0.208	VFO (PO)	0.208	*5.22	–	–	1273.6	106.40	–	352.64	29.46	–	211.2	17.64	–
2	0.0	0.278	VFO (PO)	0.278	*10.47	–	–						–			–
3	0.0	0.347	VFO (PO)	0.347	*18.59	–	–			–			–			–
4	30.0	0.000	VFO (SO)	0.066	7.74	17.31	15.50			82.15			22.75			**13.62**
5	30.0	0.208	VFO	0.231	13.35	29.88	13.53			94.16			26.07			15.61
6	30.0	0.278	VFO	0.295	15.51	34.69	13.03			97.75			27.06			16.21
7	30.0	0.347	VFO	0.361	17.75	39.70	12.60			101.10			27.99			16.77
8	30.0	0.208	VPC	0.208	12.56	28.10	13.73			92.73			25.67			15.38
9	30.0	0.278	VPC	0.278	14.92	33.37	13.16			96.80			26.80			16.05
10	30.0	0.347	VPC	0.347	17.27	38.64	12.68			100.42			27.80			16.65
11	60.0	0.000	VFO (SO)	0.159	65.53	146.60	9.09	53.20		140.14	14.73		38.80	8.82		23.24
12	60.0	0.208	VFO	0.309	85.90	192.18	8.49			149.95			41.52			24.87
13	60.0	0.278	VFO	0.355	92.15	206.15	8.35			152.61			42.25			25.31
14	60.0	0.347	VFO	0.410	99.55	222.71	8.19			155.59			43.08			25.80
15	60.0	0.208	VPC	0.208	72.21	161.54	8.87			143.58			39.76			23.81
16	60.0	0.278	VPC	0.278	81.63	182.63	8.60			148.06			40.99			24.55
17	60.0	0.347	VPC	0.347	91.06	203.71	8.37			152.16			42.13			25.23
18	103.3	0.208	VFO	0.473	415.12	928.68	5.73	30.89		222.33	8.55		61.56	5.12		36.87
19	103.3	0.278	VFO	0.510	429.66	961.21	5.68			224.25			62.09			37.19
20	103.3	0.347	VFO	0.539	441.40	987.48	5.64			225.77			62.51			37.44
21	103.3	0.208	VPC	0.208	308.29	689.68	6.17			206.39			57.15			34.23
22	103.3	0.278	VPC	0.278	336.24	752.22	6.04			210.92			58.40			34.98
23	103.3	0.347	VPC	0.347	364.20	814.76	5.92			215.17			59.58			35.68

Table 3b
Ranges of measured dissipation rates using the direct evaluation method (ε_{DE}) at different FOVs with the corresponding λ_k and Δ/λ_k values calculated using ε_{DE}.

	FOV 1			FOV 2			FOV 3		
Run (-)	ε_{DE} range (m^2 s^{-3})	λ_k range (µm)	Δ/λ_k range (-)	ε_{DE} range (m^2 s^{-3})	λ_k range (µm)	Δ/λ_k range (-)	ε_{DE} range (m^2 s^{-3})	λ_k range (µm)	Δ/λ_k range (-)
1	–	–	–	–	–	–	–	–	–
2	–	–	–	–	–	–	–	–	–
3	–	–	–	–	–	–	–	–	–
4 to 23	0.01–534.23	6.58–111.16	11.46–193.63	0.82–2532.28	4.46–33.21	10.62–79.11	2.53–813.98	5.92–25.08	8.42–35.67
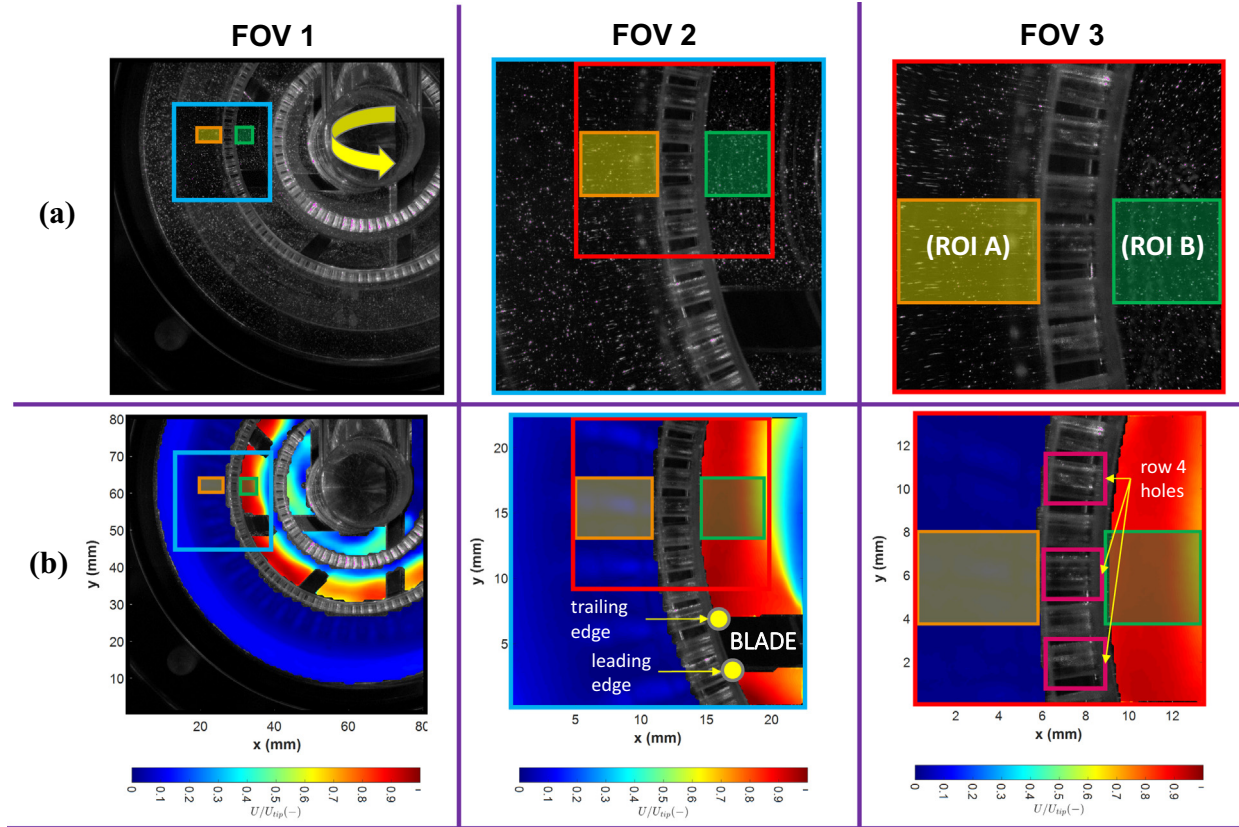
Fig. 3. Regions of interest at selected field of views FOV 1, FOV 2 and FOV 3 in: (a) raw images and (b) velocity field plots.

(Baldi and Yianneskis, 2003; Delafosse et al., 2011; Hoque et al., 2015; Xu and Chen, 2013). The fields of view selected in this work are shown in Fig. 3. Saarenrinne et al. (2001) showed that, for example, to resolve 65% and 90% of the dissipation rate with sufficient accuracy, the spatial resolution has to be 9λ_k and 2λ_k respectively, where

$$\lambda_k = \left(\frac{v^3}{\varepsilon}\right)^{1/4} \tag{3}$$

and v is the fluid kinematic viscosity and ε is the local specific energy dissipation rate. An average value for ε (power per unit mass) can be calculated using

$$\varepsilon_{avg} = \frac{P}{\rho V} \tag{4}$$

where ρ is the fluid density, V is the filled volume of the mixing head (4.47×10^{-4} m^3) (opposed to conventional rotor-swept volume) and P is the power, which for a standard 150/250 Silverson in-line high shear mixer is defined as (Cooke et al., 2012):

$$P = Po_Z \rho N^3 D_{r,o}^5 + k_1 M_T N^2 D_{r,o}^2 \tag{5}$$

where Po_Z is the 'zero flow' power constant (0.197), ρ is the fluid density, N is the rotor speed, $D_{r,o}$ is the outer rotor diameter, k_1 is a proportionality constant (9.35) and M_T is the total mass flow rate.

Calculated values of λ_k are summarised in Table 3a which shows that the highest PIV resolution achieved in the experiments at FOV 3 is ~14λ_k which implies that <65% of the energy dissipated is resolved.

The turbulent flow properties can be obtained by carrying out a Reynolds decomposition of the angle resolved velocity as proposed by Sharp and Adrian (2001). This is carried out below, for example, for the x component of velocity, U,

$$U = U'' + \overline{U}|_\theta \tag{6}$$

where $\overline{U}|_\theta$ is the angle-resolved mean and U'' is the true fluctuating turbulent velocity component since the periodic component U_p is removed by using angle-resolved measurements. Thus, for the following equations, the angle resolved RMS values for the x and y components of velocity, U and V respectively i.e.

$$U_{rms} = \sqrt{\overline{U''^2}}, V_{rms} = \sqrt{\overline{V''^2}}, \tag{7}$$

The turbulent kinetic energy or TKE (k), is the portion of the kinetic energy generated by eddies that manifest from velocity fluctuations due to turbulence. This provides a mixing mechanism via turbulent dispersion and can be evaluated from 2-D velocity using the isotropic approximation (potential impact of this assumption is discussed in Section 3.2.2):

$$k = \frac{3}{4}(U_{rms}^2 + V_{rms}^2) \tag{8}$$

Reynolds stresses arise due to momentum transfer by the fluctuating velocity field and are normally defined as $R_{ij} = \overline{U_i'' U_j''}$ which in 2-D, can be reduced to the following symmetric tensor:

$$R_{ij} = -\begin{pmatrix} \overline{U''U''} & \overline{U''V''} \\ \overline{V''U''} & \overline{V''V''} \end{pmatrix} \tag{9}$$
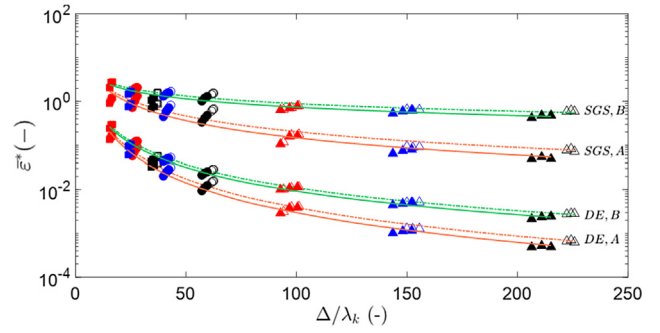
The local specific energy dissipation rate may be determined from rate of viscous dissipation of the mechanical energy (Hinze, 1975) and by applying some isotropic assumptions (local isotropy hypothesis); for 2-D data this reduces to (Sharp and Adrian, 2001):

$$\varepsilon_{DE} = \nu \left[2\overline{\left(\frac{\partial U''}{\partial x}\right)^2} + 2\overline{\left(\frac{\partial V''}{\partial y}\right)^2} + 3\overline{\left(\frac{\partial V''}{\partial x}\right)^2} + 3\overline{\left(\frac{\partial U''}{\partial y}\right)^2} + 2\overline{\frac{\partial U''}{\partial y} \cdot \frac{\partial V''}{\partial x}} \right] \tag{10}$$

This method was applied at the best achievable spatial resolution ($\sim$14 λ_K) using the velocity data from the PIV measurements. Since this is still relatively coarse, Smagorinsky closure sub-grid scale (SGS) model was also used to enable estimation of the unresolved scales (see Gabriele et al., 2009; Sheng et al. 2000). The final cross-gradient term in Eq. (10), $\overline{\frac{\partial U''}{\partial y} \cdot \frac{\partial V''}{\partial x}}$, is very small (Khan, 2005) and thus deemed negligible and hence omitted in Eq. (11).

$$\varepsilon_{SGS} = (C_S \Delta)^2 \left[4\overline{\left(\frac{\partial U''}{\partial x}\right)^2} + 4\overline{\left(\frac{\partial V''}{\partial y}\right)^2} + 2\overline{\left(\frac{\partial V''}{\partial x}\right)^2} + 2\overline{\left(\frac{\partial U''}{\partial y}\right)^2} \right]^{\frac{3}{2}} \tag{11}$$

The link between the dimensionless spatial resolution and the calculated mean specific energy dissipation rates for both ROIs using the DE method, portrayed in Fig. 4 are very similar and follow a power-law relationship e.g. $\overline{\varepsilon_{DE}^*} \propto \left(\frac{\Delta}{\lambda_k}\right)^{-2}$ with coefficient of determinations, $R^2 > 0.986$ (see Table 4). This approach is the same as that of Delafosse et al. (2011) and also takes into account an important consideration that the evaluated coefficients and exponents (Table 4) are only valid for the energy dissipation rates averaged over the selected ROI. It is also noteworthy that since λ_k was calculated using ε_{avg}, local scales are smaller in areas of high energy dissipation, which also means that Δ/λ_k can be larger in those regions. However, the intention is to demonstrate how ε measurements greatly depend on the PIV resolution. Nevertheless, the ranges of directly measured local dissipation rates ε_{DE} and the corresponding λ_k and Δ/λ_k values are reported in Table 3b. The results using SGS also follow the same general trend but also emphasise the difference (larger gap) between ROIs A and B as well as between VFO and VPC conditions. In both methods, ROI B and VFO lines are consistently higher than ROI A and VPC lines respectively. This is because higher energy dissipation is expected in regions that are subject to higher shear e.g. within the rotor swept volume (ROI B) while partially closing the valve (VPC conditions) has a dampening effect on overall energy dissipation by imposing solid body rotation (discussed in detail in Section 3.0). Moreover, as finer scales are resolved e.g. at FOV 3 in Fig. 4, the DE and SGS values begin to converge to the true dissipation rate value in both

Fig. 4. Effect of the dimensionless spatial resolution on the mean specific energy dissipation rates (non-dimensionalised with N^3D^2) calculated using Direct Evaluation, DE and Sub-grid Scale, SGS methods at the regions of interest: A (presence of jet), in orange lines and B (presence of high shear), in green lines. The combination of dash-dot (-.) lines and open symbols represent VFO conditions while solid (–) lines and filled symbols represent VPC conditions. For the symbols, colours denote rotor speeds: N = 30.0 rps (red), N = 60.0 rps (blue) and N = 103.3 rps (black) whereas shapes denote field of view: FOV 1 ($\triangle$), FOV 2 ($\bigcirc$) and FOV 3 ($\square$). (For interpretation of the references to colour in this figure legend, the reader is referred to the web version of this article.)

ROIs A and B (lines get closer together). However, the SGS method will always yield higher values as at the given conditions (especially at higher Reynolds numbers), it models for the unresolved scales unlike the DE method e.g. those below the cut-off point which is the final grid size.

Although SGS method results in higher values of energy dissipation rates, the results using the DE method are used in the discussions. This is to ensure homogeneity in the methodology used to evaluate other turbulence properties such as Reynolds stresses and turbulent kinetic energy (TKE), which use raw PIV velocity data e.g. no modelling involved. In addition, the distributions generated using both the SGS and DE methods were very similar.

3. Results

3.1. Fluid dynamics

The total mass flow rates for all experimental runs (Table 3a) are plotted in Fig. 5a. The black, blue, red and green dash-dot (-.) lines indicate the M_Ps set in the runs: 0, 0.208, 0.278 and 0.347 kg s^{-1} respectively. The open symbols represent the total mass flow rates achieved for VFO conditions and the closed symbols are for VPC conditions. When the external pump is switched off ($M_P = 0$ kg s^{-1}), the Silverson mixer can self-pump (SO conditions) up to 60.0 rps (a tip speed of 11.97 m s^{-1}) and generate a flow rate (M_S), shown by the black open symbols. This is over twice the 5 m s^{-1} tip speed achieved by Casugbo and Baker (2018) for the same mixer with similar setup and experimental condition. The pumping by the Silverson alone was possible as water can pass through the clearances between the lobes and housing in the external pump. Air entrainment occurred for rotor speeds higher than 60.0 rps as the external pump acts as a flow restriction in the suction line. This may occur for a number of reasons. One possibility is that the pressure in the Silverson drop below the vapour pressure, another may be leakage of air from the atmosphere into the low pressure zone in the mixing head via the mechanical seals. Calculation of the NPSH revealed that notwithstanding the restriction imposed, the NPSH at the highest flow rate at the external pump was 10.97 m which exceeds the required NPSH of 2.0 m. At the mixer, the NPSH was 9.44 m which suggests leakage rather than cavitation as the mechanism, but no definitive cause was identified. However, no air entrainment was observed across the experimental runs when the external pump was used in addition

Table 4
Summary of constants and exponents for $\bar{\varepsilon}_{DE} = A\left(\frac{\Delta}{\lambda_k}\right)^b$ (Fig. 4).

ROI (-)	Flow class (-)	Method (-)	constant A (-)	exponent b (-)	R^2 (-)
A	VFO	DE	86.01	−2.19	0.987
A	VPC	DE	95.37	−2.25	0.987
B	VFO	DE	33.66	−1.76	0.994
B	VPC	DE	34.32	−1.78	0.986
A	VFO	SGS	50.65	−1.21	0.901
A	VPC	SGS	59.99	−1.31	0.926
B	VFO	SGS	12.96	−0.59	0.922
B	VPC	SGS	13.60	−0.63	0.917
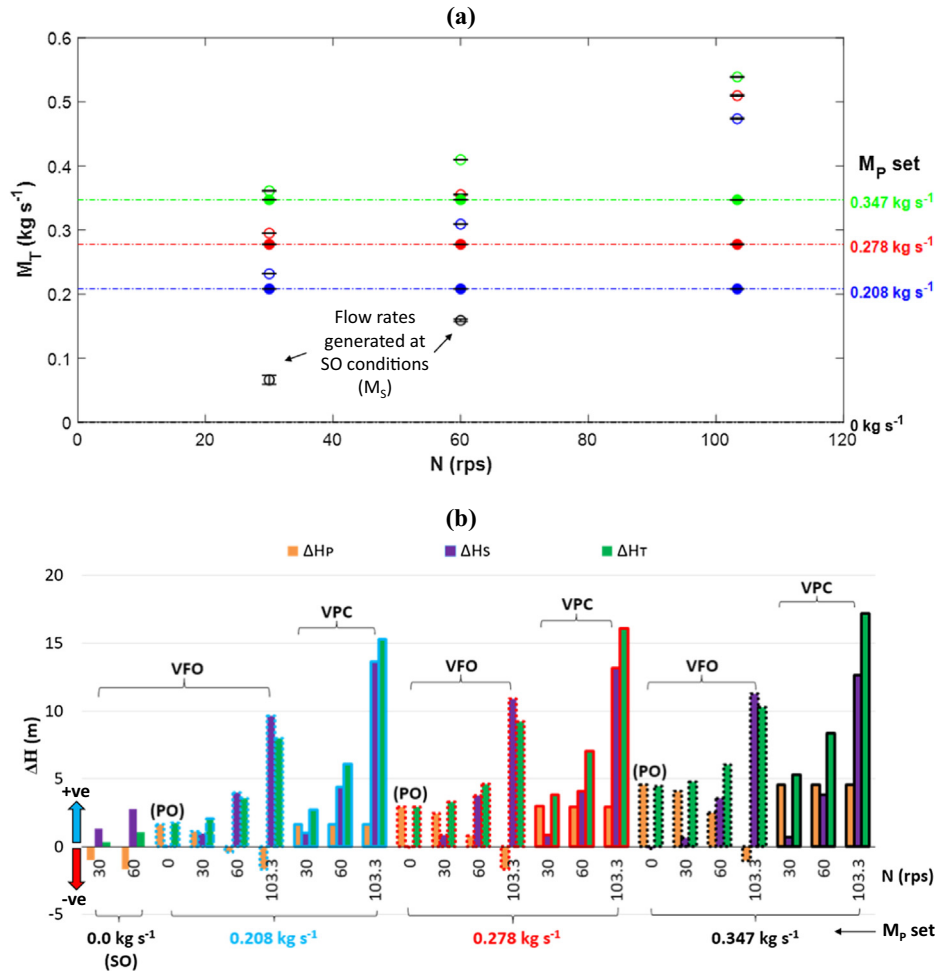
Fig. 5. (a) Total mass flow rates achieved in experimental runs. Open and closed symbols indicate data points for VFO and VPC conditions respectively. Blue, red and green horizontal dash-dot (-.) lines are drawn to emphasise that at VPC conditions, $M_T = M_P$ (b) Total head delivered by the external pump and Silverson in all experimental runs.

to the Silverson. Furthermore, system curves for VFO and VPC conditions, superimposed with the measured heads delivered by the pump and Silverson showed that the NPSH requirements were met in all experimental runs.

It is evident through Fig. 5a that higher flow rates are attained at increased M_P and N. Espinoza et al. (2018) observed that the flows were predominantly radial at high pump flow rate (M_P) and tangential at high Silverson rotor speed, N. Since the pump and Silverson are arranged in series (Fig. 1), the mass flowing through the system is equal to M_T (combined flow rates generated by Silverson (M_S) and external pump (M_P)) and the relative contributions of the Silverson and external pump which drive the overall flow regime are a function of total head profile through the pipework (Fig. 5b). The total head is the sum of the total dynamic heads

(static head + dynamic head) generated by the pump and Silverson: $\Delta H_T = \Delta H_P + \Delta H_S$. In addition, volumetric flow rate, Q_T (M_T/ρ) was used to follow conventions in plotting system and pump performance curves.

It is clear from Fig. 5b that when the external pump is used solely (PO, N = 0 rps), the total head delivered (green bars) is generated mostly by the external pump (orange bars) thus, the flow in the mixing head is predominantly radial (Fig. 6a). When the Silverson is used alone (SO), unsurprisingly it provides the majority of the total head for SO conditions (purple bars) hence the flow is predominantly tangential and there is hardly any jetting (Fig. 6h). Moreover, Fig. 5b shows that negative head occurs when the external pump is switched off and it acts as a flow restriction. For VFO and VPC conditions, it can be seen that the relative contributions

by the external pump and Silverson vary according to the process parameters set. At constant M_P, for both VFO (bars with dashed (--) line border) and VPC (bars with solid (-) line border) conditions, the Silverson mixer contributes more head as N is increased. However, the contribution by the external pump at VFO conditions decreases down to a negative value, showing that it still acts as a flow restriction when the external pump flow rate is exceeded by the pumping capacity of the Silverson. The rate of decline decreases when M_P is increased (compare decline of orange bars at constant 0.208 kg s^{-1} and 0.347 kg s^{-1}). Finally, for VFO and VPC conditions that have similar M_T e.g. for VFO: N = 60.0 rps; M_P = 0.278 kg s^{-1} (red open symbol in Fig. 5a) and for VPC: N = 60.0 rps; M_P = 0.347 kg s^{-1} (green closed symbol in Fig. 5a), the pressure drop across the Silverson mixer (purple bars for corresponding conditions in Fig. 5b) is more or less the same, which implies that the flow patterns are also very similar (compare Figs. 9 and 10 for the corresponding conditions). This suggests that pressure drop across the mixing head governs the local flow patterns inside it.

The influence of changing N at constant M_P and vice versa is shown in Fig. 6. Fig. 6b and c show that when N was increased at constant M_P, the region of higher velocities (red) in the rotor swept volume increased (top right of each plot with green arrows) and the jets get weaker (in terms of penetrating the bulk as although the jet exit hole velocity has increased, it does not penetrate the bulk as effectively as in PO conditions (Fig. 6a) because it moves more in the tangential direction) whereas the opposite is true when M_P was increased at constant N (compare Fig. 6c and d). The weakening effect on the jet is also more apparent at VPC con-

ditions especially at low M_P and higher rotor speeds (compare Fig. 6f and g). These observations imply that there is a compromise between N and M_P and is discussed further below with regards to Fig. 8.

For VPC conditions, the contribution of the external pump is shown as constant and positive at constant M_P and gradually increases as M_P was increased (compare orange bars of equal heights to the M_P set (PO bars) in Fig. 5b). This was expected as the increased backpressure ensured that the positive displacement pump delivered a constant flow rate at a certain head and pump speed. This also suggests that the radial flow profile is fixed at constant M_P thus the strength of jets depended on the rotor speed. For instance, by comparing Fig. 6e and g, jets significantly diminish to a point where the flow pattern resembles that for a SO condition (Fig. 6h) although it is important to note that the outlet valve opening (number of turns open) differs with varying rotor speeds for a constant M_P. Finally, it is noteworthy that the values of total head delivered at VPC conditions are consistently higher than the corresponding VFO conditions which implies that energy is lost when overcoming additional resistance imparted by the valve. This is emphasised in Fig. 7 which portrays the system head profiles for varying process conditions at locations defined in Fig. 1. It shows that the gap between VFO (open symbols, dashed lines) and VPC conditions (closed symbols, solid lines) is more significant at higher rotor speeds. It is also noteworthy that after the Silverson e.g. between locations E and F, there is an increase in head due to back pressure losses imposed by the pipework of the recycle loop (1″ diameter, 4.55 m flexible braided pipe).
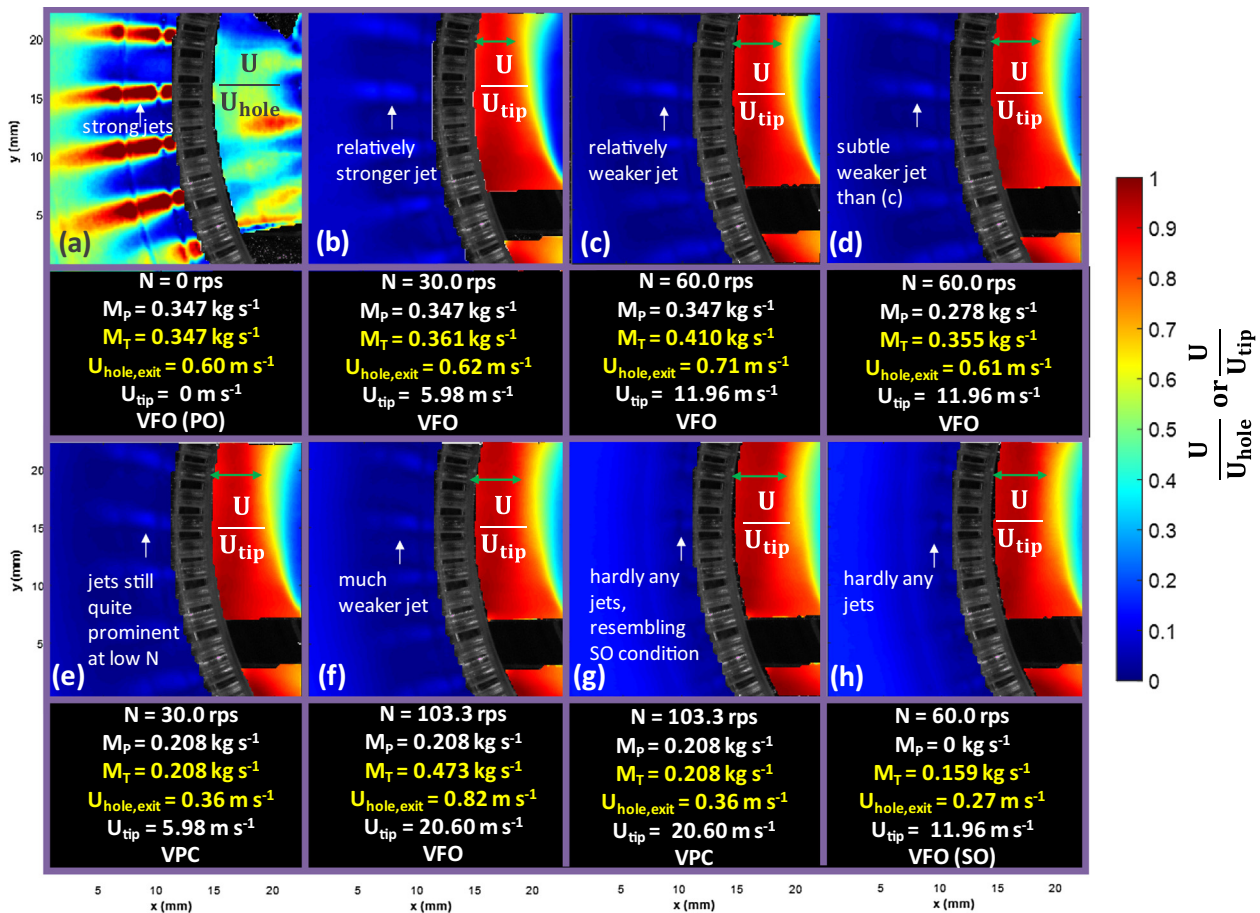

Fig. 6. Velocity field plots at different experimental runs.

Fig. 8 shows the relative contributions of the external pump ($\Delta H_P/\Delta H_T$ – circles and orange lines) and Silverson mixer ($\Delta H_S/\Delta H_T$ – squares and purple lines) to the total head delivered in VFO (Fig. 8a) and VPC (Fig. 8b) conditions at varying rotor speeds and M_P set (symbol colours). The orange and purple lines were drawn to guide the eyes where the crossover of overall flow control is between the pump and the Silverson mixer at the 0.5 line (red dash-dot (.-) line) at constant M_P (same symbol colours). For instance, once $\Delta H_S/\Delta H_T > 0.5$, it is presumed that the Silverson dominates and generates a more tangential flow while the contrary is true when $\Delta H_P/\Delta H_T > 0.5$. It is evident that in both VFO and VPC conditions, the external pump only dominates the process flowrate and hence flow patterns at really low rotor speeds e.g. at N = 0 (PO conditions in Fig. 8a) and 30.0 rps (Fig. 8a an b) (all the circle symbols are above 0.5). At intermediate rotor speeds, the Silverson mixer progressively takes over the flow and completely dominates at very high rotor speeds (all the square symbols are above 0.5).

Looking at the VFO data points in Fig. 8a, the point of crossover (**X** symbols) occurs at higher rotor speeds at increasing M_P set e.g. from ~32 rps at 0.208 kg s^{-1} to ~54 rps at 0.347 kg s^{-1}. This demonstrates the relative competition between the pump and the Silverson mixer at varying process conditions. Partially closing the valves (Fig. 8b) pushes these boundaries further to the right e.g. ~38 rps at 0.208 kg s^{-1} to ~66 rps at 0.347 kg s^{-1} and ensures that the contribution of both the pump and Silverson mixer are positive. For example at N = 103.3 rps, the Silverson mixer does not have to work harder in overcoming the restriction imposed by the pump at VFO conditions (square symbols > 1 and circle symbols < 0). However, this is not necessarily an advantage as although throttling the valve lowers the NPSH, energy is wasted in trying to overcome the additional resistance. Moreover, this promotes fluid recirculation (solid body rotation) and leads to an increase of temperature in the mixing head. At PO conditions, the Silverson mixer also acts as a restriction but not as significantly. Finally, these plots
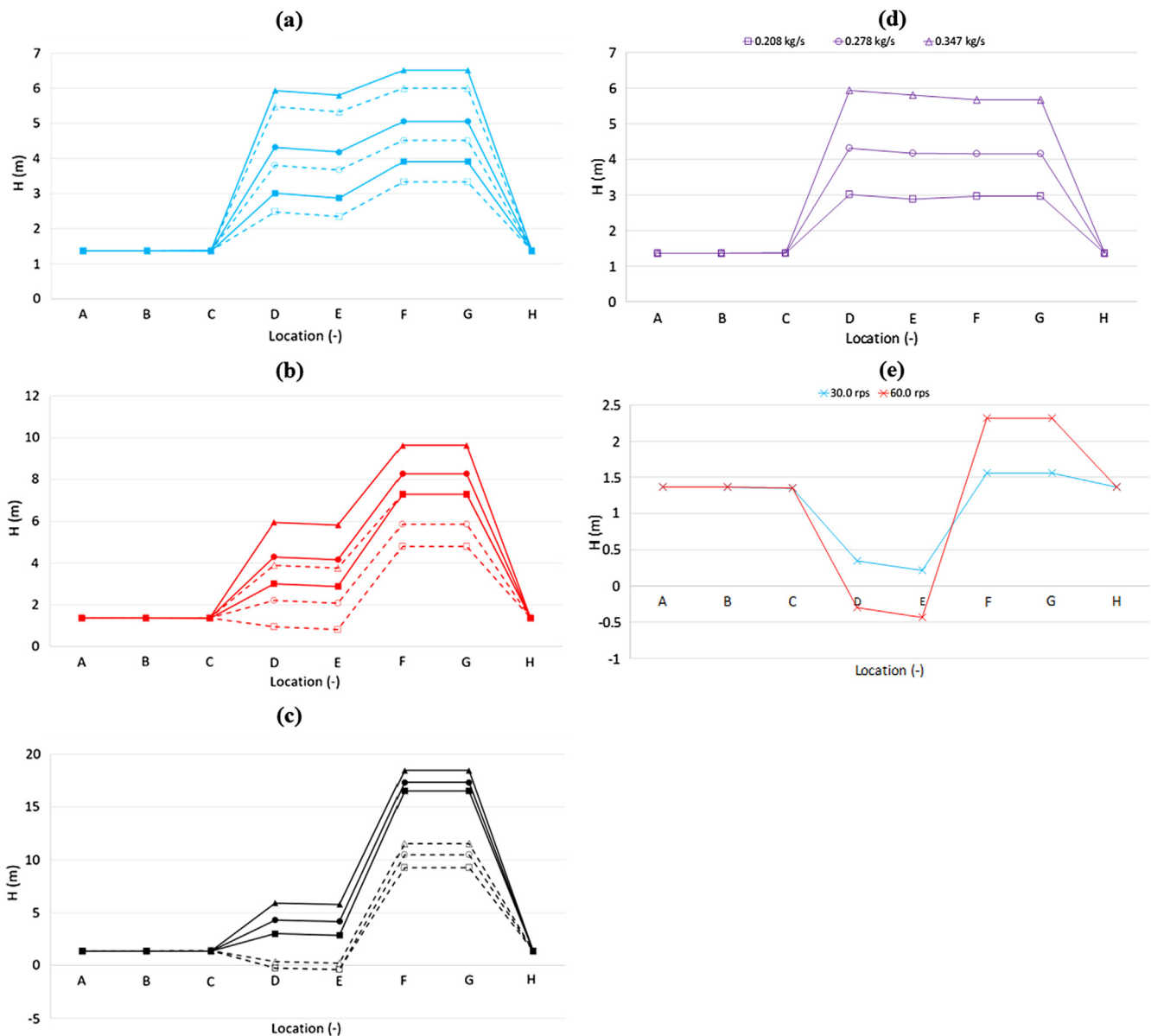

Fig. 7. Head profiles at locations defined in Fig. 1 for VFO and VPC conditions at fixed rotor speeds (a) 30.0 rps (b) 60.0 rps and (c) 103.3 rps. Symbols colours denote rotor speeds: N = 30.0 rps (blue), N = 60.0 rps (red) and N = 103.3 rps (black). Shapes denote external pump flow rate set, M_P = 0.208 kg s^{-1} (□), M_P = 0.278 kg s^{-1} (○), M_P = 0.347 kg s^{-1} (△). Open and closed symbols as well as dashed (–) and solid (-) lines indicate data points for VFO and VPC conditions respectively Head profiles for PO and SO conditions are shown in (d) and (e) respectively. (For interpretation of the references to colour in this figure legend, the reader is referred to the web version of this article.)
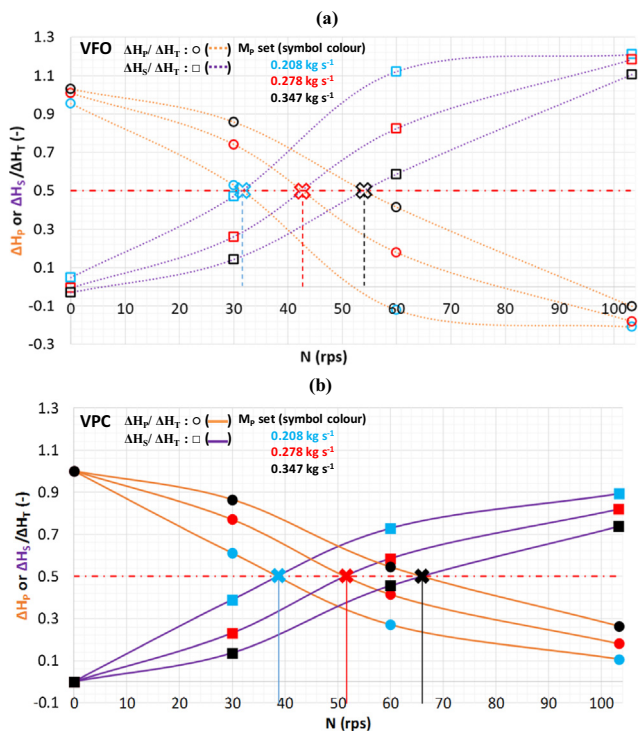
Fig. 8. Contribution of pump and Silverson on the total head delivered at (a) VFO and (b) VPC conditions. Colours denote external pump flow rates: $M_P = 0.208$ kg s^{-1} (blue), $M_P = 0.278$ kg s^{-1} (red), $M_P = 0.347$ kg s^{-1} (black). Shapes and lines denote head contribution by the pump: ΔH_P (○, orange line) and Silverson, ΔH_S (□, purple line). Lines are to guide the eyes only to give an indication where the change of dominance occurs, denoted by (X) symbols at the 0.5 red dash-dot (-.) line. (For interpretation of the references to colour in this figure legend, the reader is referred to the web version of this article.)

can be useful in applications e.g. emulsification processes where essential knowledge of how much the pump and Silverson mixer influence the flow is required.

3.2. Energy dissipation

3.2.1. Effect of N and M_T on regions of maximum ε

Energy dissipation plots calculated from the highest resolution measurements made (FOV 3) are shown in Figs. 9 and 10 for VFO and VPC conditions respectively. The figures are designed to show the effect of increasing M_P at constant N (rows) and vice versa (columns). The maximum value of ε in the colour bar for each row in the figures (i.e. at constant N) is set to the maximum value in ROI A.

The figures show that, unsurprisingly, energy dissipation rate increases with N at constant M_P. As the rotor rotates anticlockwise, as N increases it can be observed that the angle of the jets emanating through the stator holes changes in the direction of rotation (purple arrows). This effect is more significant at lower M_P (first column in Fig. 9) and when the valve is partially closed (Fig. 10). Additionally, the intensity of energy dissipation in the jets are lower at VPC conditions, implying that the tangential motion of the fluid causes the energy to be re-distributed to the surrounding fluid more uniformly (or moves as a solid body, losing energy as heat). In ROI B, the distribution of energy dissipation in the area near the primary stator appears to be dependent on N for both VFO and VPC conditions.

Another interesting observation is the presence of low energy dissipation behind the rotor blade (blue boxes in Figs. 9 and 10) and high-energy dissipation near the outer primary stator (right

edge of the plots in Figs. 9 and 10). The latter could be attributed to the interaction of fluid behind the blade with the jets emanating from the primary stator, whilst, the former could be due to the fluid attaching onto the upstream face of the rotor blade, as observed by Sparks (1996). This observation is also apparent in the work by Jasińska et al. (2015). Since the PIV measurements are angle resolved, it can be seen that this low energy dissipation region extends with increasing rotor speed and occurs more rapidly at VPC conditions (blue boxes in Figs. 9 and 10), which, again, implies the onset of solid body rotation which is not desired in mixing/emulsification. Moreover, this also reveals that there are sweet spots of high energy dissipation rate at the inner wall of the secondary stator (magenta circles in Figs. 9 and 10) which also recede with increasing N.

A hypothesis that trailing vortices form behind the rotor blade (on either side), similar to that in Rushton Disk Turbines in stirred vessels, is also considered. This is confirmed by the vorticity, Q criterion and swirl strength (λ_{CI}) plots in Fig. 11. The vortex near the inner wall of the outer stator is dissipated by the perforated stator wall (otherwise, a phenomenon called tip leakage vortex similar to those in turbomachinery and centrifugal pump with solid wall casings will manifest), which is supported by weak energy dissipation in the adjacent stator hole (purple boxes in Figs. 9 and 10). The vortex on the other side of the blade then interacts with the jets emanating from the primary stator. This phenomenon is not fully understood but may be important for potential break up mechanisms.

In Fig. 9, it is evident in ROI A that at constant N, increasing M_P intensifies and spreads the maximum energy dissipated through the jets (red circles in Fig. 9). Additionally, doing so drives the jet angle towards the clockwise direction (purple arrows). The flow becomes more radial for both VFO and VPC conditions since the contribution of the pump to the total head also increases with M_P (Fig. 5b). As for ROI B, the areas of high energy dissipation e.g. in close proximity to the primary stator and in the inner wall of the secondary stator, bridge together to a greater degree with increasing M_P especially for VFO conditions at lower N (green box in Fig. 9). These results suggest that an optimal match between N and M_P has to be found to maximise areas of high energy dissipation rates within the mixing head.

Close-up plots of energy dissipation within ROIs A and B are shown in Fig. 12. These respective areas corresponding to the emanating jets and high shear region have been identified by (Ashar et al., 2018; Atiemo-Obeng and Calabrese, 2004; Håkansson, 2018; Thapar, 2004) as areas where break up of droplets is most likely to occur. The following observations apply to all runs that have both the Silverson mixer and external pump in operation. Run 13 with N = 60.0 rps and $M_P = 0.278$ kg s^{-1} is used as a reference to illustrate flow patterns in the ROIs in Fig. 12 as a function of whether the outlet flow is unrestricted (VFO) or restricted (VPC). The velocity vectors show that fluid recirculation occurs in ROI A and is stronger under VFO conditions, which is also reflected by the stronger dissipation rate. The jets in VFO conditions are stronger and more uniform, resembling those for PO conditions (see Fig. 6a) and are weaker in VPC condition as the flow inside the mixing head becomes more tangential, similar to SO conditions (see Fig. 6h). In ROI B, the fluid flows in the direction of rotation as it is within the rotor swept region. These results are consistent with the findings of Espinoza et al. (2018). There are three distinct levels of energy dissipation in this region shown in the figure: I – intermediate dissipation near the inner wall of the secondary stator, II – lower dissipation in between regions I and III, and III – higher dissipation further to the right near to the emanating jets from the primary stator. The difference between VFO and VPC conditions for this particular run is small but becomes dramatic at higher rotor speeds. This could be due to a more uniform dissipation of
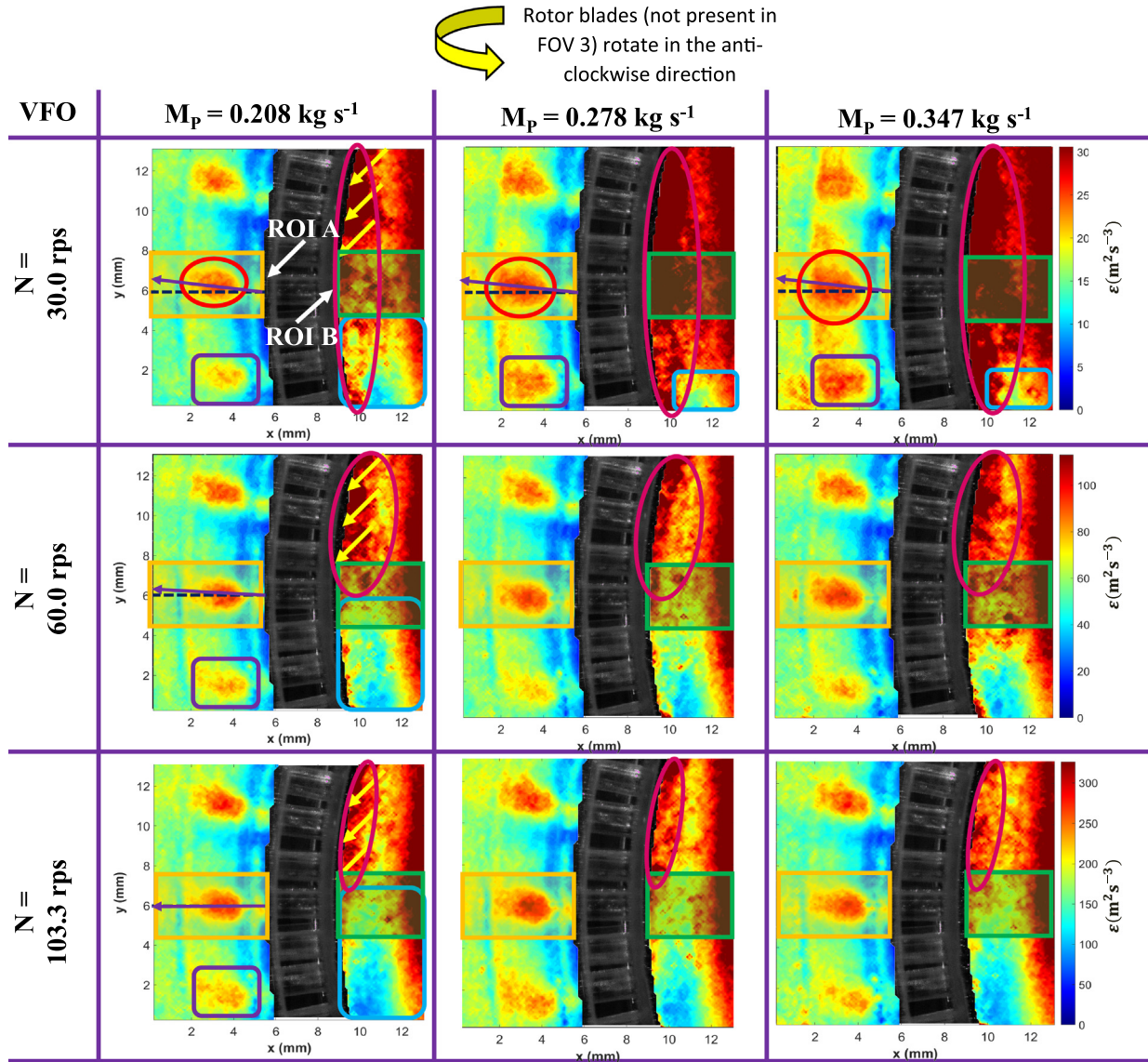
Fig. 9. Local specific energy dissipation rate distributions calculated by the direct evaluation (DE) method for VFO conditions in FOV 3.

energy across the whole mixing head promoted by increased tangential motion of the fluid which results in better transfer of momentum or it could be perceived as poor mixing due to the onset of solid body rotation. The latter is supported by the increased head at VPC conditions (Fig. 5b and 8) and suggests that energy is lost to heat due to the recirculation of the fluid caused by the increased resistance at the outlet. Either way, increasing the rotor speed and partially closing the outlet valve results in lower ε in localised areas.

3.2.2. Dependencies on N and M_T

Table 5 and Fig. 13a imply that $\overline{\varepsilon_{DE,A}} \propto N^{1.77-1.90}$ and $\overline{\varepsilon_{DE,B}} \propto N^{1.59-1.72}$ which do not follow the conventional $\varepsilon \propto N^3$ as established in the literature, mainly because only a fraction of the total energy dissipation has been resolved. The same was found with the SGS results which exhibited very similar trends, suggesting that the trends are correct but not the absolute values. The exponents are $\overline{\varepsilon_{SGS,A}} \propto N^{2.66-2.84}$ and $\overline{\varepsilon_{SGS,B}} \propto N^{2.42-2.61}$ but still do not equal 3. The only main difference between the DE and SGS distribution plots is that the relative values are higher for SGS as this

method models the unresolved scales. This can be attributed to the fact that the measurements were made in 2D and so the third component of velocity had to be calculated using the isotropy assumption. In addition, the finest spatial resolution used with the DE method of ~14λ_K is $\gg 2\lambda_K$ and considering that high shear mixers can generate droplet sizes lower than λ_K, it is inevitable that the exponents will be underestimated (Saarenrinne et al., 2001). Moreover, as the turbulence intensity increases e.g. at higher ε, the length scales get smaller hence more is missed by the DE method (lower exponents than SGS). The same applies for SGS as it is also very sensitive to the PIV resolution e.g. it models more effectively with better measurements (Håkansson et al., 2017c). This analogy also explains why the exponents in ROI B are less than that in ROI A as the flow in the former is more turbulent. Furthermore, it also has to be taken into account that these exponents apply to their respective ROIs only e.g. it does not take into account the entire mixing head volume or area. These suggest that the relationship between ε and N is not the same across the whole mixing head, supporting the claims by Thapar (2004) and Sparks (1996) that different loca-
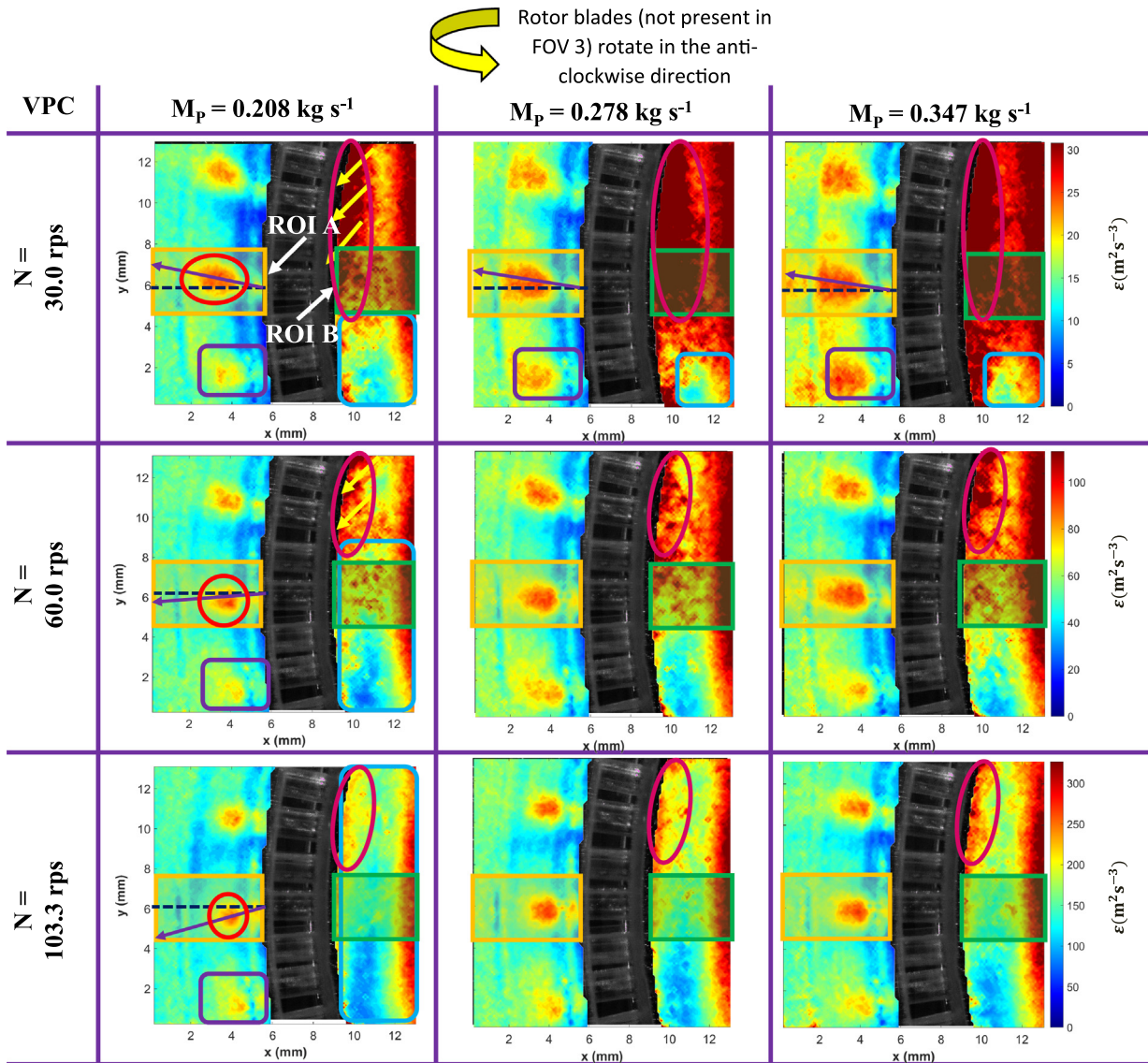
Fig. 10. Local specific energy dissipation rate distributions calculated by the direct evaluation (DE) method for VPC conditions in FOV 3.

tions in the mixing head may be locally laminar or turbulent due to the complex geometry within the mixer.

The maximum values of energy dissipation obtained in this study (in the hundreds for DE, or thousands for SGS) are comparable to the lower end of the range of simulated values obtained in an existing CFD study (k-ε model) by Jasińska et al. (2015) for the same Silverson model (Case III). In a similar region, the simulated values of energy dissipation at a constant rotor speed of N = 100 rps and a range of total mass flowrate (of water) M_T = 0.167 to 0.667 kg s^{-1} ranges from ~152 to 124,000 m^2 s^{-3}. To the best knowledge of the authors, these results have not been validated with experimental measurements which would have been useful as a comparison for this work. However, it is important to note the differences between the experimental setup as the modelled system in the CFD study did not have an external pump in the loop and thus not accounted for. In addition, the Silverson mixer was gravity fed and its flow rate was solely regulated by an outlet valve.

Another point of view regarding the $\varepsilon \propto N^a$ relationship is through the relationship $P \propto N^b$ which is relevant as $\varepsilon \propto P$. Thapar (2004) stated that determination of the flow regime can be done by investigating the dependency of the unit's power draw on rotational speed e.g. if exponent b is 3, turbulent conditions apply otherwise if it is 2 then laminar conditions apply. This implies that energy dissipation rate at different locations in the mixing head will have a different dependency on the rotor speed depending on whether the flow is laminar or turbulent. On the other hand, Hall (2012) attributes the difference in b values to the different terms in the power draw equation for the same mixer (Eq. (5)). The first term on the right hand side is due to fluid resistance which is analogous to a stirred vessel and is proportional to N^3 whereas the second term is due to fluid acceleration inside the mixing head, which is proportional to N^2D^2. The b values he evaluated are between 2.26 and 2.67 which he compared to that of Bourne and Studer (1992) ~2.5. He then concluded that the resulting values are due to the combined effects of the first and second terms in Eq. (5). Furthermore, his b values decreased with increasing flow rate indicating the greater impact of the squared flow rate term on the total power draw at increased M_T. The b values determined in this work (Table 5) e.g. 1.59 to 1.90 for DE and 2.42 to 2.84 for SGS, reflect the same trend and are in the same range and magnitude.
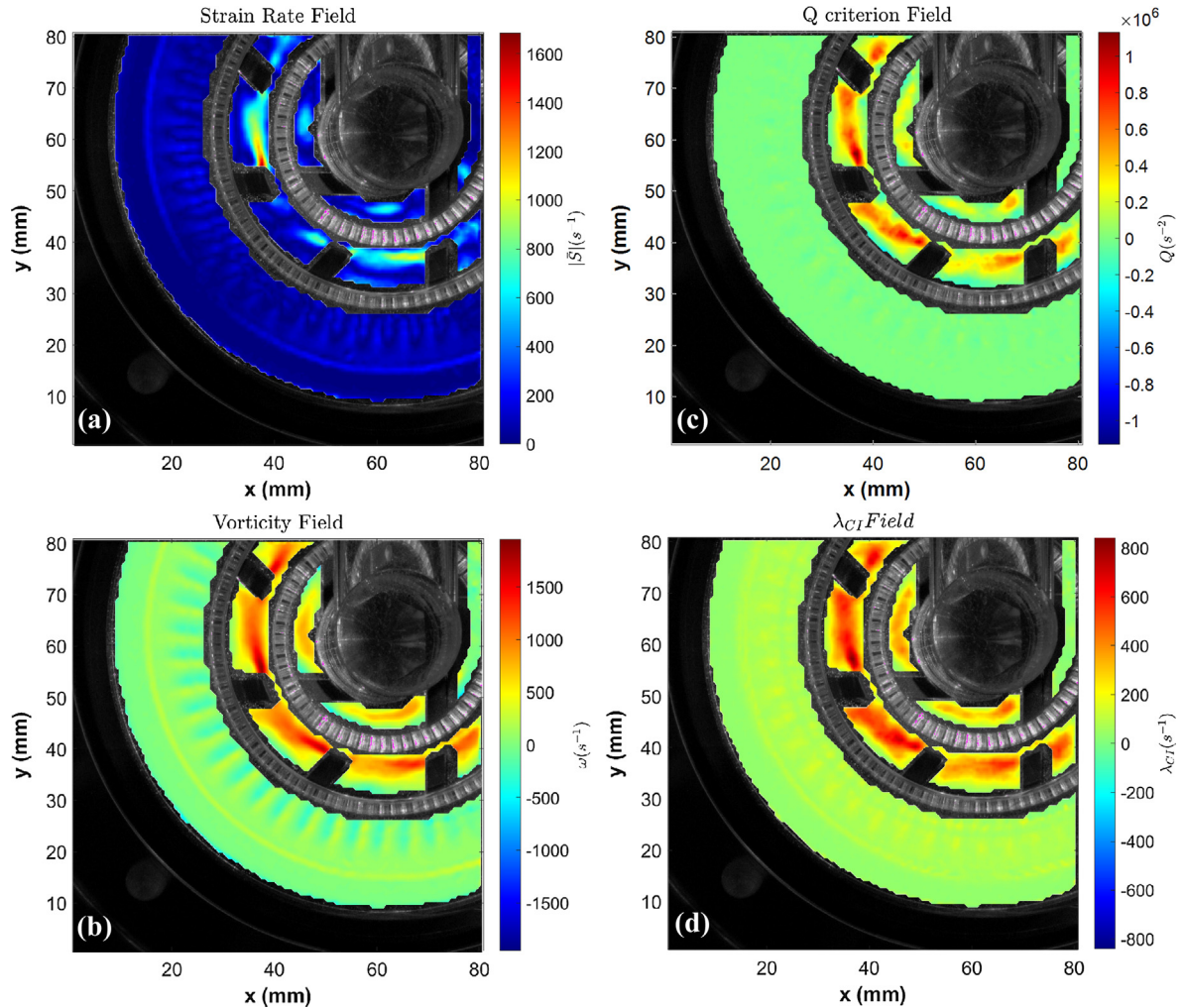
Fig. 11. Contour plots of (a) Rate-of-Strain (RoS) (b) Vorticity (c) Q criterion and (d) λ_{CI} (swirling strength) criterion for process condition combination of N = 60.0 rps; M_P = 0.278 kg s^{-1}; VFO at FOV 1.

Finally, the effect of the total mass flow rate, M_T on energy dissipation rates in ROIs A and B calculated using the DE method is portrayed in Fig. 13b. At constant N, M_T is always higher in VFO conditions as the combined flow rate was not restricted to the initially set M_P as in the VPC conditions. Nevertheless, all data points fall on the same line and display a linear relationship (see Table 6 for exponents). The values for ROI B are always higher than in ROI A, i.e. in the high shear region. The gap between ROI A and ROI B lines increases with N as there is more energy input into the system thus more energy is dissipated and more so in ROI B. Furthermore, the lines have low gradients at lower rotor speeds, meaning that dissipation values can be treated constant and indicates that M_T is only influential at very high rotor speeds which agrees with the findings of Hall et al. (2011). The dip at higher N from VFO to VPC, again, suggests that partially closing the valve results in overall lower energy dissipation (most likely due to heat loss by fluid recirculation/solid body rotation) e.g. by a factor of ~0.20 (250 to 200 m^2 s^{-3}) in ROI B and ~0.14 (175 to 150 m^2 s^{-3}) in ROI A at N = 103.3 rps and thus affecting ROI B more significantly (compare Fig. 9 with Fig. 10).

3.3. Reynolds stresses and TKE

It is expected that areas of high energy dissipation rates are also areas of high TKE and Reynolds stresses (Fig. 14). Knowing where stresses are localised is vital in determining potential droplet break up mechanisms. In ROI A, the highest value of R_{11} is in the core of the jets for both VFO and VPC conditions (orange box in Fig. 14), caused by the presence of dominant x-velocity components emanating from the stator hole. The area of higher values is larger for VFO (2 < x < 4 mm; 5.75 < y < 6.5 mm) in comparison with that for VPC (3 < x < 4 mm; 6 < y < 6.25 mm). Away from the jets, the values approach zero. For R_{22}, the highest values are still in the core of the jets for both VFO and VPC conditions but are lower in magnitude by about half the maximum of R_{11}. The y-velocity components from the jets are lower than the x-velocity components. The magnitude of the maximum R_{12} is much lower for both VFO and VPC conditions e.g. about a tenth of the maximum of R_{11}, suggesting that the shear is negligible. It is, however, interesting to see that shear stresses are higher in VPC conditions as the tangential motion of the fluid is increased, suggesting increased interaction between the bulk fluid and the emanating jet. Moreover, the fluid from the preceding jet directly enters the core of the succeeding jet, as opposed to going around the recirculation zones prior to reaching the jet core as in the VFO condition (Fig. 12).

In ROI B, areas of high R_{11} (green box in Fig. 14) have similar magnitude as in ROI A and resemble the regions defined in Fig. 12. Region I has higher ε due to the x-velocity component of the fluid impinging on the inner wall of the secondary stator. Region II has lower ε as it is within the area behind the blade while
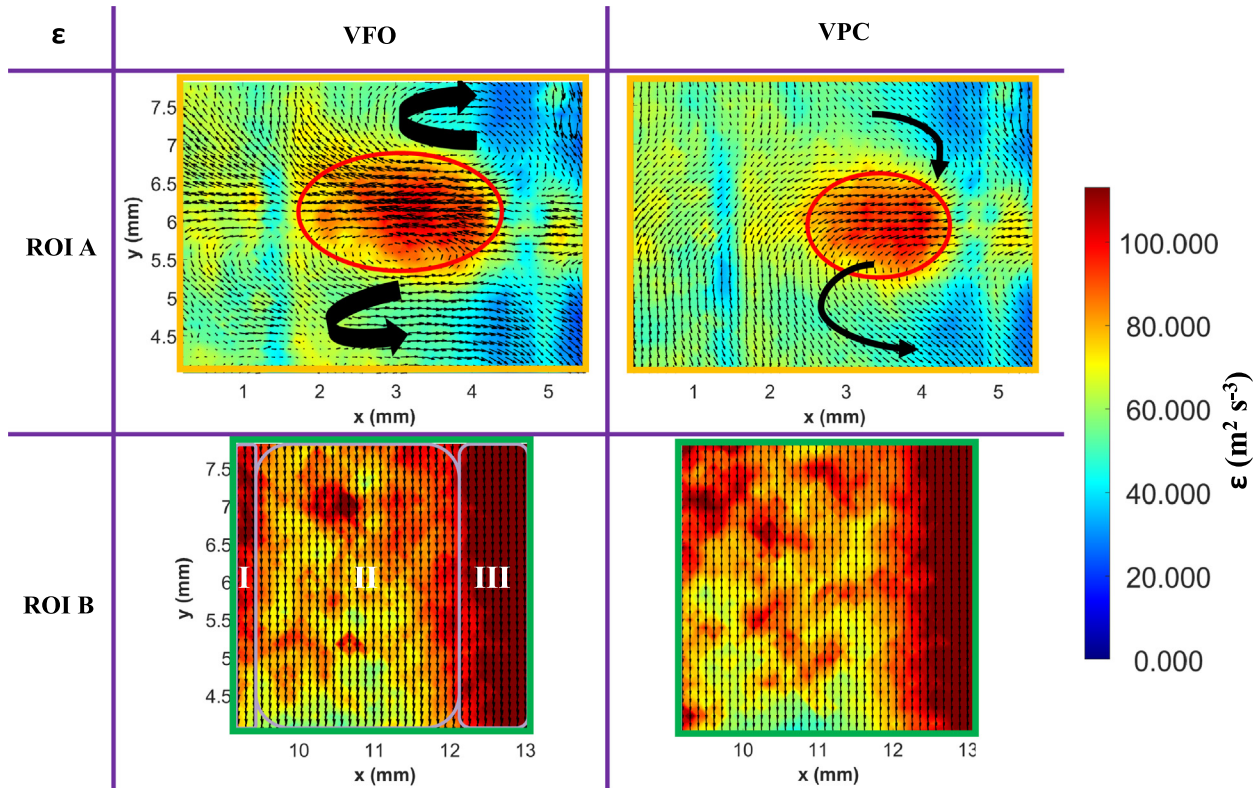
Fig. 12. Local specific energy dissipation rates calculated by direct evaluation (DE) method with accompanying vectors for the process condition combination of 60.0 rps; 0.278 kg s^{-1} at ROIs A and B in FOV 3 (left column: VFO; right column: VPC).

Table 5
Summary of constants and exponents for $\bar{\varepsilon} = AN^b$ (Fig. 13a).

ROI (-)	External pump flow rate, M_P (kg s^{-1})	Method (-)	constant A (-)	exponent b (-)	R^2 (-)
A	0.208	DE	0.023	1.90	0.996
A	0.278	DE	0.032	1.84	0.997
A	0.347	DE	0.043	1.77	0.998
B	0.208	DE	0.075	1.72	0.990
B	0.278	DE	0.129	1.61	0.993
B	0.347	DE	0.141	1.59	0.996

Region III also has higher ε due to the x-velocity components of the jets from the primary stator interacting with the fluid within the area between the primary and secondary stators. R_{11} values are slightly higher in VFO conditions especially in the area near the primary stator as the jet flows are less affected by relatively weaker tangential flow. Areas of high R_{22} are an order of magnitude higher than both the maximum values of corresponding R_{11} and R_{12}, which means that it dominates in ROI B. This makes sense as it is within the rotor swept volume, meaning that the majority of the fluid flows in the direction of rotation i.e. y-velocity components in the downwards direction. Finally, as with ROI A, R_{12} has very little influence in this region.

From these observations, it can be deduced that R_{11} and R_{22} dominate in ROIs A (squares in Fig. 15a) and B (circles in Fig. 15b) respectively (although their values are of the same magnitude and do not differ significantly, conveying some validity of the isotropic assumptions) especially at higher N and M_P. R_{12} can be treated negligible in both regions. In addition, they also influence the ε values in these regions (Fig. 15c and d). Furthermore, they also dictate the TKE values in ROIs A and B (Fig. 14) since $k = \frac{3}{4}\left(U_{rms}^2 + V_{rms}^2\right)$ which is equivalent to $k = \frac{3}{4}(R_{11} + R_{22})$. It then

follows that high TKE results in high ε (Fig. 16b). TKE is always higher in ROI B and at increasing N (Fig. 16a) as the flow in this region is turbulent e.g. it is within the rotor swept volume where Re $\geq$ 120,000.

Fig. 16a shows the relationships between N and TKE in ROIs A and B. For ROI A, it was deduced that $k \propto N^{1.8}$ (Table 7) which is as expected as $k \propto N^2$ (Eq. (5)). Conversely, it is more complicated for ROI B e.g. a second order polynomial (which is expected) and a linear fit were used for VFO and VPC conditions respectively (Table 7). This can be explained by referring to ε plots in Figs. 9 and 10 for the process conditions where the differences are greatest e.g. at N = 103.3 rps and at constant M_P. For the VFO conditions in ROI B, at constant N = 103.3 rps, the distributions of ε (and hence TKE) look very similar hence why the data points (encircled red) in Fig. 16a are clustered together. For VPC, the distributions are also very similar but are weaker in magnitude. As for constant M_P at 0.278 kg s^{-1} (blue line in Fig. 16a), for VFO conditions, as N increases, areas of high ε diminish as low ε extends behind the blade which is more dramatic for VPC conditions. This is why the data points for VFO and VPC are very different at N = 103.3 rps (black arrow,
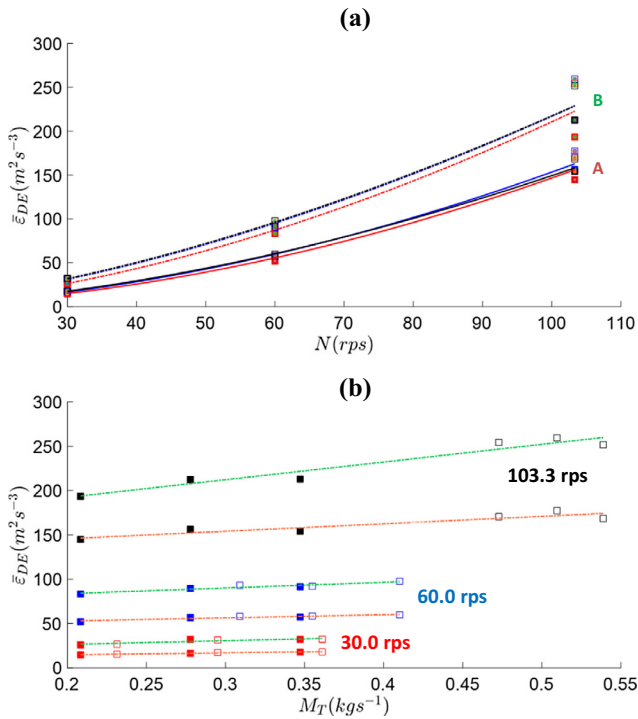
Fig. 13. Influence of (a) rotor speed, N and (b) total mass flow rate, M_T on the mean local specific energy dissipation rates calculated using the Direct Evaluation (DE) method at the regions of interest: A (presence of jet), in solid (–) lines and B (presence of high shear), in dash-dot (-.) lines in FOV 3. Open and closed symbols represent VFO and VPC conditions respectively. Symbol colours denote external pump flow rate: M_P = 0.208 kg s^{-1} (red), M_P = 0.278 kg s^{-1} (blue) and M_P = 0.347-kg s^{-1} (black). (For interpretation of the references to colour in this figure legend, the reader is referred to the web version of this article.)

Fig. 16a). The same trend applies for all other conditions with constant M_P. Ultimately, the relationship (equation of the curve) depends on what is captured in the ROI e.g. for ROI B, the distribution of high ε will depend on N, the higher it is, the lower ε is due to solid body rotation.

4. Discussion

With the current knowledge of Reynolds stress, TKE and ε distributions, as well as calculated Reynolds numbers and nominal residence times (τ_R), defined in Table 8 at probable locations (Fig. 17), it can be deduced that droplet break up locations and potential break up mechanisms in the mixing head are similar to those identified by Thapar (2004).

In the stator hole and R-S gap, simple shear and elongational stresses may apply as the flow is laminar due to the small length scale. The τ_R of droplets in the R-S gap is very short which implies

that it is bypassed by many droplets which break further in the stator hole. However, τ_R in the stator hole is also very short thus the drops have insufficient time to be sheared/elongated and split (deformation time > τ_R). In the turbulent regions such as in the inlet pipe, rotor and volute, the drops break due to the dissipation of TKE, primarily in the inertial subrange. This is a reasonable assumption as it was found that ε is proportional to at least the square of N, approaching N^3, which convey that the dominating disruptive stress is the inertial stress (Ashar et al., 2018). Furthermore, the residence times of the droplets are longer in these regions, providing the drops greater probability to break. In addition, the distributions plots for constant M_P (Fig. 18) of the calculated local turbulence number, Re_T ($k^2/\varepsilon v$), local integral length scales (ILS), L ($k^{3/2}/\varepsilon$) and Kolmogorov length scales, λ_k ($(v^3/\varepsilon)^{1/4}$), using the directly measured k and ε via DE method, support this. It is evident that the spatial distribution of Re_T is similar across the rotor speeds, with the higher values seeming to spread out more and increase in magnitude as N increases. The same trend is observed for ILS distribution, which is as expected as it represents the highest energy containing large eddies in the regions of high turbulence. It then follows that these same regions are where the smallest scales (blue regions) are found in the λ_k distribution (which are very similar across the rotor speeds with the same order of magnitude) e.g. where the jets penetrate the volute and within the gap between the primary and secondary stators. Moreover, smaller scales also tend to reside near the inner wall of the secondary stator and within the proximity of the primary stator where jets from it penetrate the fluid within the primary-secondary stator gap. These make sense as λ_k decreases with increasing Reynolds number and also that larger eddies (ILS) cascade their energy to the lowest scales of turbulence (λ_k).

From the above observations, it can be concluded that dissipation of TKE is the main driving force for droplet break up in in-line HSMs. The proposed break up sequence can be described by considering the streamlines (velocity vectors) that the drops may follow and comparing areas of high ε in the mixing head. The droplet may be conveyed into the bulk flow induced by the rotor within the area bounded by the secondary stator via the inlet pipe; it may then collide with the inner stator wall and subsequently sheared in the stator holes. Eventually, they emanate from the holes and are subjected to deformation stresses within the jets that interact with the bulk flow in the volute. This also occurs between the primary and secondary stators. Therefore, in relation to the findings on how the process parameters affected Reynolds stress, TKE and ε distributions, their possible effects on droplet break up, are identified as follows:

- The maximum value of ε, especially in ROI B will increase with N, but at the expense of more confined regions of 'sweet spots'. This means that droplets may be subject to greater disruptive forces in these regions but are less likely to visit them. This therefore emphasises the importance of simultaneously considering both the hydrodynamics and distribution of disruptive

Table 6
Summary of constants and exponents for $\bar{\varepsilon} = AM_T + c$ (Fig. 13b).

ROI (-)	Rotor speed, N (rps)	Method (-)	constant A (-)	constant c (-)	R^2 (-)
A	30.0	DE	22.61	10.14	0.936
A	60.0	DE	35.39	45.77	0.852
A	103.3	DE	84.12	128.87	0.863
B	30.0	DE	42.07	18.00	0.772
B	60.0	DE	64.12	70.87	0.878
B	103.3	DE	199.48	152.41	0.934

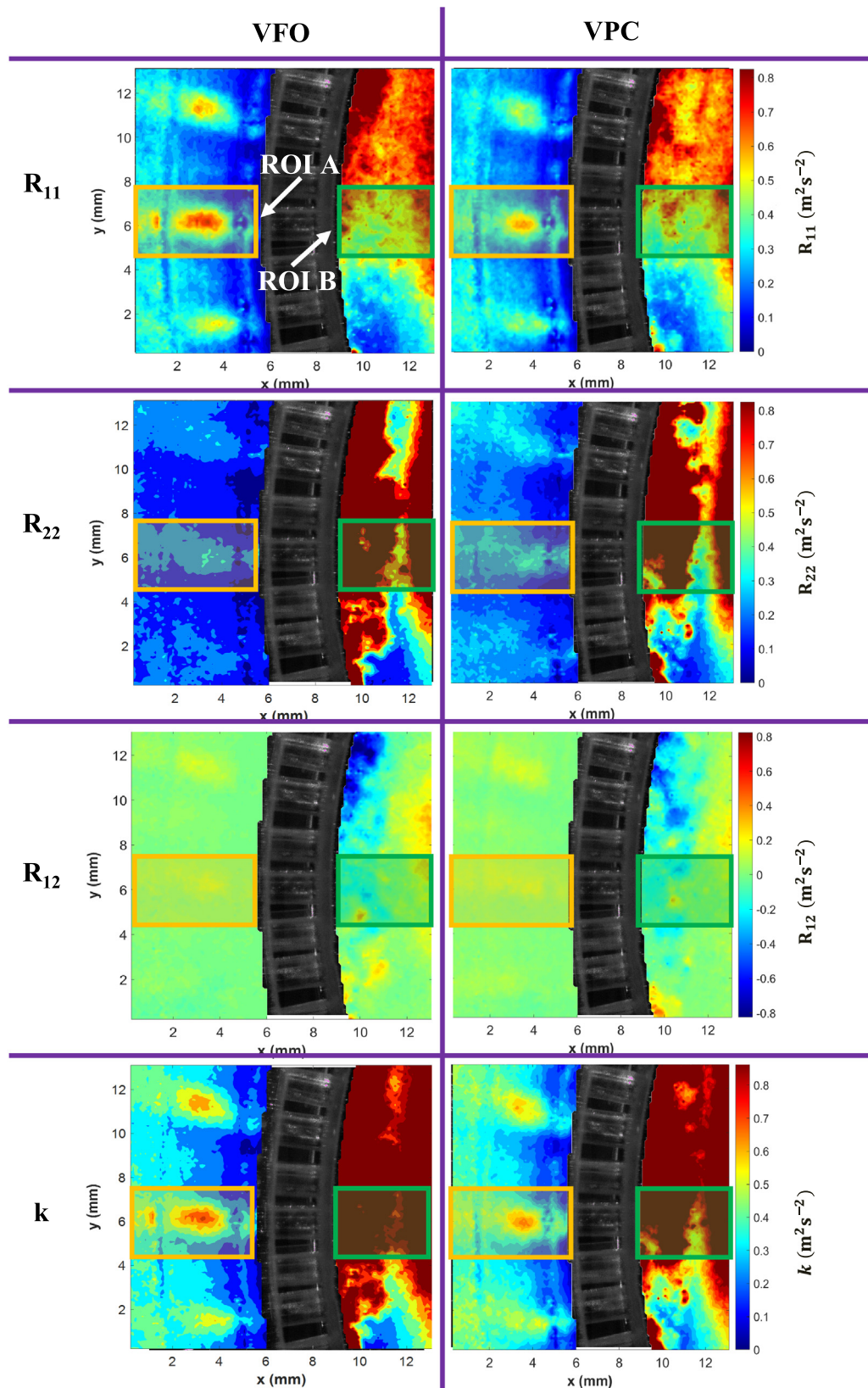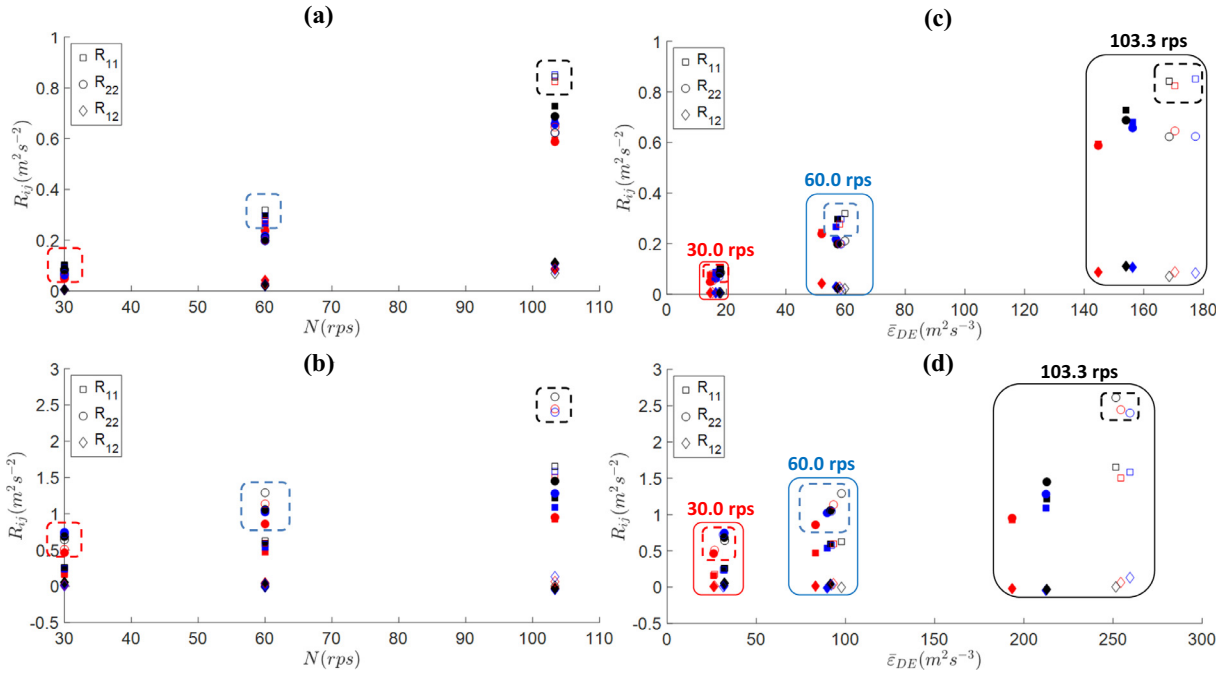**Fig. 14.** Reynold stresses (R_{11}, R_{22} and R_{12}) and turbulent kinetic energy, k plots in FOV 3 for the process condition combination of 60.0 rps; 0.278 kg s^{-1}.

Fig. 15. (a) Influence of rotor speed on Reynolds stresses (R_{11}, R_{22} and R_{12}) in ROI A, (b) Influence of rotor speed on Reynolds stresses in ROI B. Corresponding plots of the relationship between local specific energy dissipation rates and Reynold stress components in (c) ROI A and (d) ROI B. In all plots, open and closed symbols represent VFO and VPC conditions respectively and symbol colours denote external pump flow rate: M_P = 0.208 kg s^{-1} (red), M_P = 0.278 kg s^{-1} (blue) and M_P = 0.347 kg s^{-1} (black). (For interpretation of the references to colour in this figure legend, the reader is referred to the web version of this article.)
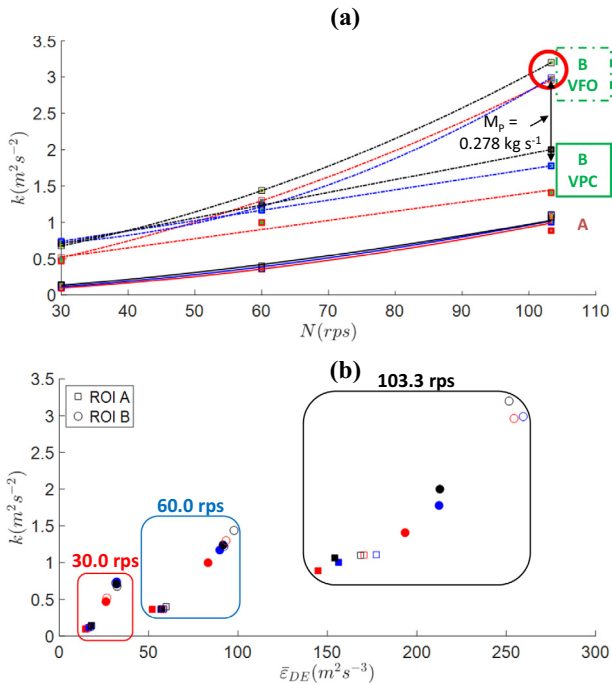
Fig. 16. (a) Influence of rotor speed on turbulent kinetic energy at ROIs A (presence of jet), in solid (−) and B (presence of high shear), in dash-dot (-.) lines in FOV 3 and; (b) Relationship between local mean specific energy dissipation rates (calculated using DE method) and turbulent kinetic energy. In both plots, open and closed symbols represent VFO and VPC conditions respectively and symbol colours denote external pump flow rate: M_P = 0.208 kg s^{-1} (red), M_P = 0.278 kg s^{-1} (blue) and M_P = 0.347 kg s^{-1} (black). (For interpretation of the references to colour in this figure legend, the reader is referred to the web version of this article.)

forces in the mixing head (Ashar et al., 2018). Furthermore, partially closing the outlet valve impose the same effects at an accelerated rate as it induces a greater tangential motion, promoting solid body rotation (wasted energy) which results in larger areas of the mixing head with medium ε. This is evident in Fig. 10.

- Increasing M_P yields stronger jets and promotes interaction with the surrounding fluid (better turbulence). However, caution must be taken as suggested by Sparks (1996) not to end up with a 'drowned suction'. A mismatch between the process flow rate (M_P) and Silverson flow rate (M_S) must be avoided (Casugbo and Baker, 2018).

Finally, agitator shear rate also has a contribution, as shown in the RoS plot in Fig. 11, but as expected, high levels are concentrated within the rotor swept volume. Finally, results support the claim that the R-S gap does not significantly influence droplet break up (Atiemo-Obeng and Calabrese, 2004).

5. Conclusions

Angle-resolved PIV measurements were taken on a 150/250 in-line Silverson high shear mixer to define its turbulence characteristics and propose a method on quantifying the contribution of the external pump and Silverson mixer in driving the flow in the system and thus the mixing head as well as potential droplet break up mechanisms. Turbulence parameters such as Reynolds stresses, TKE and energy dissipation rates (via direct evaluation (DE) and large eddy PIV sub-grid scale (SGS) methods) were quantified and observed how they were influenced by the process parameters.
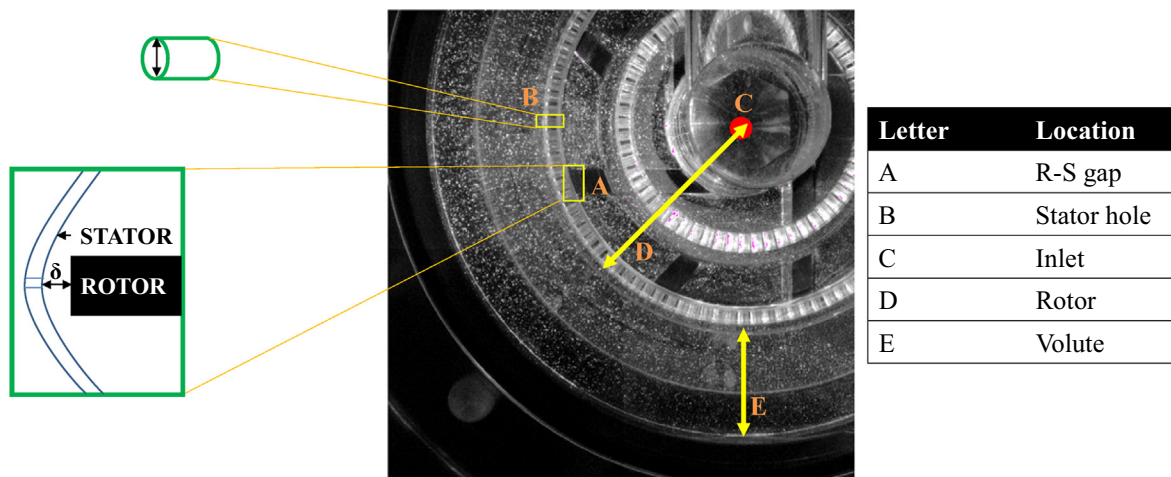
Table 7
Summary of constants and exponents for $k = AN^b + C$ or $k = AN^2 + DN + E$ (Fig. 16a).

ROI (-)	External pump flow rate, M_P (kg s^{-1})	Method (-)	Flow class (-)	constant A (-)	exponent b (-) *constant C (-) ˣconstant D (-)	^constant E (-)	R^2 (-)
A	0.208	DE	VFO + VPC	0.0002	1.88	–	0.995
A	0.278	DE	VFO + VPC	0.0003	1.78	–	0.996
A	0.347	DE	VFO + VPC	0.0005	1.65	–	0.994
B	0.208	DE	VFO	0.0002	*0.011	^0.036	1.000
B	0.278	DE	VFO	0.0003	*−0.013	^0.823	1.000
B	0.347	DE	VFO	0.0002	*0.007	^0.289	1.000
B	0.208	DE	VPC	0.0126	ˣ0.146	–	0.969
B	0.278	DE	VPC	0.0142	ˣ0.314	–	1.000
B	0.347	DE	VPC	0.0176	ˣ0.180	–	1.000

Table 8
Ranges of Reynolds numbers and residence times at different locations in the mixing head.

	L (m)	U (m s^{-1})	Re Range	τ_R (s)
Inlet pipe	$D_{inlet} = 0.01905$	$U_{inlet} = 0.73–0.89$	$\frac{\rho U_{inlet} D_{inlet}}{\mu} = 14,000 - 36,000$	$\frac{V_{inlet}}{M_T/\rho} = 0.029 - 0.075$
Rotor	$D_{ss,outer} = 0.0635$	$U_{tip} = 5.98–20.61$	$\frac{\rho ND^2}{\mu} = 120,000 - 420,000$	$\frac{V_{rotorswept}}{M_T/\rho} = 0.271 - 0.701$
Stator hole	$D_h = 0.00159$	$U_{hole} = 0.36–0.94$	$\frac{\rho U_{hole} D_h}{\mu} = 600 - 1,500$	$\frac{V_{hole}}{M_{hole}/\rho} = 0.004 - 0.011$
R-S gap	$\delta = 0.00024$	$U_{tip} = 5.98–20.61$	$\frac{\rho N\delta}{\mu} = 7,200 - 25,000$	$\frac{V_\delta}{M_T/\rho} = 0.001 - 0.004$
Volute (jets)	Distance from outer wall of secondary stator to the inner wall of the mixing head = 0.019835	$U_{jet} = U_{hole} = 0.36–0.94$	$\frac{\rho U_{hole} D_{volute}}{\mu} = 7,200 - 19,000$	$\frac{V_{volute}}{M_T/\rho} = 0.721 - 1.866$

Letter	Location
A	R-S gap
B	Stator hole
C	Inlet
D	Rotor
E	Volute

Fig. 17. Probable locations of droplet breakup.

Flow in the mixing head is radially and tangentially dominated at high pump flow rates and high rotor speeds respectively. Both co-exist at relative strengths depending on the mixer and pump settings. Furthermore, partially closing the outlet valve also promotes a more tangential flow. Two main regions of interest: jet region (ROI A) and high shear region (ROI B) were investigated to study how energy dissipation was influenced by the process parameters. It was found that areas of high ε are also areas of high Reynolds stresses and TKE. In ROI A, radial flow dominates due to the emanating jets from the secondary stator (driven by the external pump) hence most of the energy is dissipated through the jet cores. As the flow becomes more tangential at higher rotor speeds, these jets become weaker and vice versa when the external pump flow rate is increased. Drops could therefore break through elongational stresses in this region. In contrary for region B, tangential flow dominates as it is in the rotor swept volume. As the flow in this region is highly turbulent, droplet break up occurs due to turbulent stresses in the inertial sub-range. Areas of high ε or 'sweet

spots' manifest due to the proposed phenomena: (a) fluid impaction on the inner wall of the secondary stator and (b) interactions between the undisturbed vortex that forms behind the rotor blade and the jets emanating from the primary stator. However, at higher rotor speeds, although the maximum value of ε increases, the number of 'sweet spots' reduces and the area of low energy dissipation behind the rotor blade extends. To alleviate this, the external pump flow rate can be increased to allow deeper jet penetration from the primary stator into the region between the primary and secondary stators. This implies that increasing the rotor speed and partially closing the valve induces solid body rotation, which in effect decreases ε.

Energy dissipation rates were found to be proportional to $N^{1.59−1.90}$ and $N^{2.42−2.84}$ using DE and SGS methods respectively at the best attained spatial resolution ($\sim 14\lambda_K$). Both methods yielded exponents that are approaching the value of, but do not equal 3 that is well established in the literature. This is because both methods are subject to the isotropic turbulence assumption which
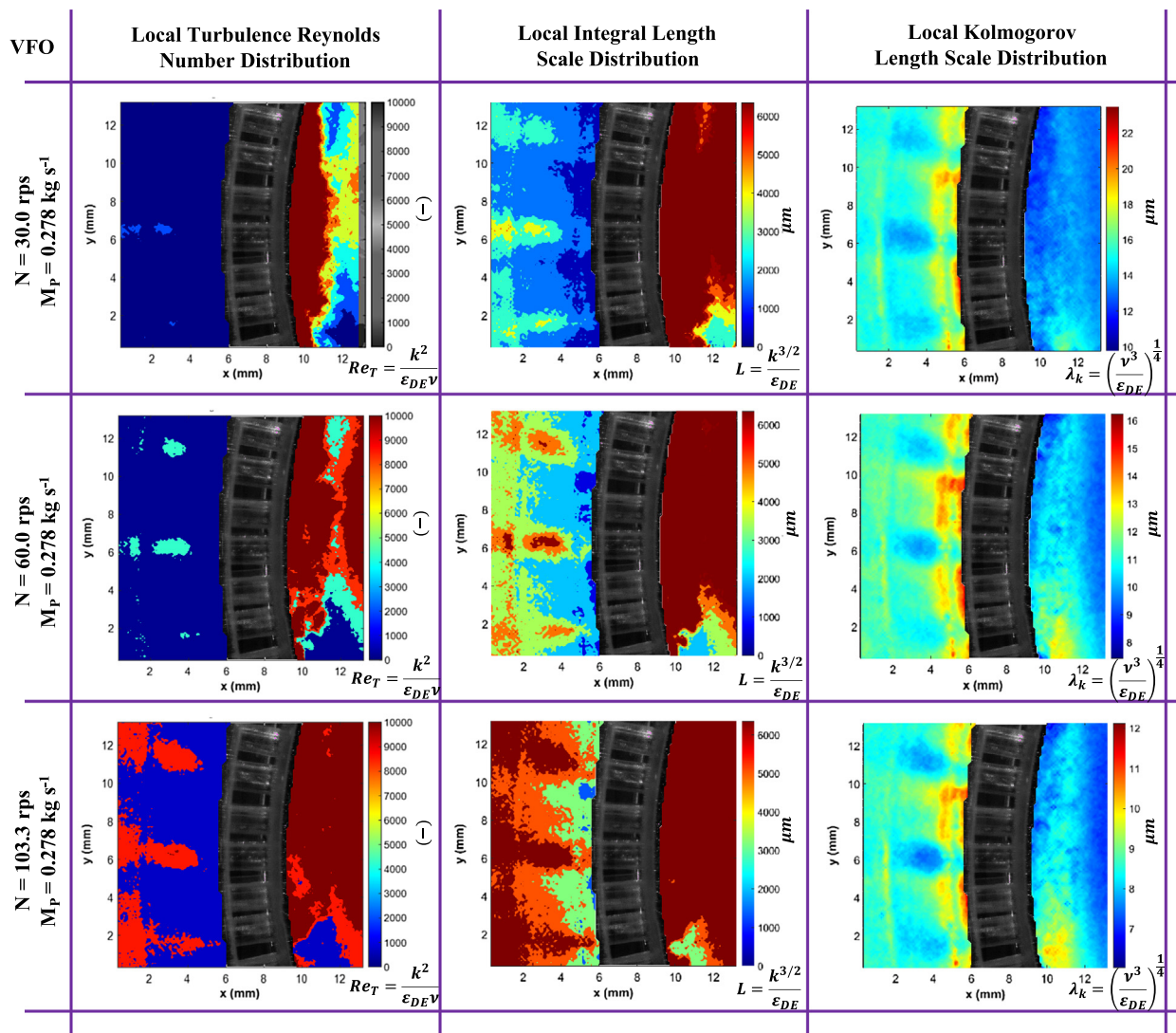
Fig. 18. Distributions plots of the calculated local turbulence number, Re_T $(k^2/\varepsilon\nu)$, local integral length scales, L $(k^{3/2}/\varepsilon)$ and Kolmogorov length scales, λ_k $((\nu^3/\varepsilon)^{1/4})$ using the directly measured k and ε via the DE method. The maximum Reynolds number for the colour bar is set to 10,000 (condition for fully turbulent flow in stirred tanks). The maximum L for the colour bar is set to D/10 (6350 μm).

means that since the data is from 2-D PIV, the missing z component had to be approximated, leading to the underestimation of the exponent. Moreover, both methods, especially DE, are also sensitive to the PIV resolution. For instance, as the turbulence intensifies at increasing ε, the length scales get smaller and thus more is missed in the measurements. The effect is worse for the DE method as it does not model for length scales below the cut-off resolution. Finally, the dependency of the energy dissipation rate with the process conditions is highly influenced by the location in the mixing head since both laminar and turbulent conditions co-exist due to the complex flow patterns in the mixing head and thus ε is not proportional to N^3 throughout the mixing head. Despite these, the evaluated exponents are within the same range in existing literature between 2.26 and 2.67 for in-line HSMs (Bourne and Studer, 1992; Hall, 2012).

CRediT authorship contribution statement

C.J.U. Espinoza: Conceptualisation, writing, review and editing.
F. Alberini: Conceptualisation, writing, review and editing.
O. Mihailova: Conceptualisation, writing, review and editing.

A.J. Kowalski: Conceptualisation, writing, review and editing.
M.J.H. Simmons: Conceptualisation, writing, review and editing.

Declaration of Competing Interest

The authors declare that they have no known competing financial interests or personal relationships that could have appeared to influence the work reported in this paper.

Acknowledgements

References

Adrian, R.J., 1986. Image shifting technique to resolve directional ambiguity in double-pulsed velocity. Appl. Opt. 25 (21), 3855–3858.

Ahmed, U., Michael, V., Hou, R., et al., 2018. An energy transport based evolving rheology in high-shear rotor–stator mixers. Chem. Eng. Res. Des. 133, 398–406.

Ashar, M., Arlov, D., Carlsson, F., et al., 2018. Single droplet breakup in a rotor-stator mixer. Chem. Eng. Sci. 181, 186–198.

Atiemo-Obeng, V.A., Calabrese, R.V., 2004. Rotor-stator mixing devices. In: Paul, E.L., Atiemo-Obeng, Victor A., Kresta, Suzanne M. (Eds.), Handbook of Industrial Mixing. John Wiley & Sons, Inc., pp. 479–505.

Baldi, S., Yianneskis, M., 2003. On the direct measurement of turbulence energy dissipation in stirred vessels with PIV. Ind. Eng. Chem. Res. 42 (26), 7006–7016.

Bourne, J.R., Studer, M., 1992. Fast reactions in rotor-stator mixers of different size. Chem. Eng. Process. Process Intensif. 31 (5), 285–296.

Carrillo De Hert, S., Rodgers, T.L., 2017. Continuous, recycle and batch emulsification kinetics using a high-shear mixer. Chem. Eng. Sci. 167, 265–277.

Casugbo, C., Baker, M.R., 2018. Pumping capacity of inline dynamic mixers and its effect on process flow control. Chem. Eng. Res. Des. 132, 982–988.

Cooke, M., Rodgers, T.L., Kowalski, A.J., 2012. Power consumption characteristics of an in-line silverson high shear mixer. AIChE J. 58 (6), 1683–1692.

Delafosse, A., Collignon, M.-L., Crine, M., et al., 2011. Estimation of the turbulent kinetic energy dissipation rate from 2D-PIV measurements in a vessel stirred by an axial Mixel TTP impeller. Chem. Eng. Sci. 66, 1728–1737.

Espinoza, C.J.U., Simmons, M.J.H., Alberini, F., et al., 2018. Flow studies in an in-line Silverson 150/250 high shear mixer using PIV. Chem. Eng. Res. Des. 132, 989–1004.

Gabriele, A., Nienow, A.W., Simmons, M.J.H., 2009. Use of angle resolved PIV to estimate energy dissipation rates for up- and down-pumping pitched blade agitators in a stirred tank. Chem. Eng. Sci. 64 (1), 126–143.

Håkansson, A., 2018. Rotor-stator mixers: from batch to continuous mode of operation—a review. Processes 6 (4), 32.

Håkansson, A., Andersson, R., Mortensen, H.-H., et al., 2017a. Experimental investigations of turbulent fragmenting stresses in a rotor-stator mixer. Part 2. Probability distributions of instantaneous stresses. Chem. Eng. Sci. 171, 638–649.

Håkansson, A., Arlov, D., Carlsson, F., et al., 2017b. Hydrodynamic difference between inline and batch operation of a rotor-stator mixer head – A CFD approach. Can. J. Chem. Eng. 95 (4), 806–816.

Håkansson, A., Innings, F., 2017. The dissipation rate of turbulent kinetic energy and its relation to pumping power in inline rotor-stator mixers. Chem. Eng. Process. 115, 46–55.

Håkansson, A., Mortensen, H.H., Andersson, R., et al., 2017c. Experimental investigations of turbulent fragmenting stresses in a rotor-stator mixer. Part 1. Estimation of turbulent stresses and comparison to breakup visualizations. Chem. Eng. Sci. 171, 625–637.

Hall, S., 2012. Scale-up of Emulsification in In-line Rotor-stator Mixers PhD Thesis. University of Birmingham, UK.

Hall, S., Cooke, M., El-Hamouz, A., et al., 2011. Droplet break-up by in-line Silverson rotor–stator mixer. Chem. Eng. Sci. 66, 2068–2079.

Hinze, J.O., 1955. Fundamentals of the hydrodynamic mechanism of splitting in dispersion processes. AIChE J. 1 (3), 285–289.

Hinze, J.O., 1975. Turbulence, an introduction to its mechanism and theory. McGraw-Hill.

Hoque, M.M., Sathe, M.J., Mitra, S., et al., 2015. Comparison of specific energy dissipation rate calculation methodologies utilising 2D PIV velocity measurement. Chem. Eng. Sci. 137, 752–767.

James, J., Cooke, M., Kowalski, A., et al., 2017a. Scale-up of batch rotor-stator mixers. Part 2—Mixing and emulsification. Chem. Eng. Res. Des. 124, 321–329.

James, J., Cooke, M., Trinh, L., et al., 2017b. Scale-up of batch rotor–stator mixers. Part 1—Power constants. Chem. Eng. Res. Des. 124, 313–320.

Jasińska, M., Bałdyga, J., Cooke, M., et al., 2013. Application of test reactions to study micromixing in the rotor-stator mixer (test reactions for rotor-stator mixer). Appl. Therm. Eng. 57, 172–179.

Jasińska, M., Bałdyga, J., Cooke, M., et al., 2015. Specific features of power characteristics of in-line rotor–stator mixers. Chem. Eng. Process. 91, 43–56.

Karbstein, H., Schubert, H., 1995. Developments in the continuous mechanical production of oil-in-water macro-emulsions. Chem. Eng. Process. Process Intensif. 34 (3), 205–211.

Khan, F.R., 2005. Investigation of Turbulent Flows and Instabilities in a Stirred Vessel using Particle Image Velocimetry PhD Thesis. Loughborough University.

Khan, F.R., Rielly, C.D., Hargrave, G.K., 2004. A multi-block approach to obtain angle-resolved piv measurements of the mean flow and turbulence fields in a stirred vessel. Chem. Eng. Technol. 27 (3), 264–269.

Kim, J.W., 2015. Comparison between Particle Image Velocimetry Data and Computational Fluid Dynamics Simulations for an In-line Slot and Tooth Rotor-stator Mixer MSc Thesis. University of Maryland, College Park, MD, USA.

Kowalski, A.J., Cooke, M., Hall, S., 2011. Expression for turbulent power draw of an in-line Silverson high shear mixer. Chem. Eng. Sci. 66 (3), 241–249.

Minnick, B.A., Kim, J.W., Ko, D.I., et al., 2018. Flow and power characteristics of an axial discharge rotor-stator mixer. Chem. Eng. Res. Des. 136, 477–490.

Mortensen, H.H., Calabrese, R.V., Innings, F., et al., 2011. Characteristics of batch rotor–stator mixer performance elucidated by shaft torque and angle resolved PIV measurements. Can. J. Chem. Eng. 89 (5), 1076–1095.

Mortensen, H.H., Innings, F., Håkansson, A., 2017. The effect of stator design on flowrate and velocity fields in a rotor-stator mixer—An experimental investigation. Chem. Eng. Res. Des. 121, 245–254.

Mortensen, H.H., Innings, F., Håkansson, A., 2018. Local levels of dissipation rate of turbulent kinetic energy in a rotor–stator mixer with different stator slot widths—An experimental investigation. Chem. Eng. Res. Des. 130, 52–62.

Padron, G.A., 2001. Measurement and Comparison of Power Draw in Batch Rotor-stator Mixers MSc Thesis. University of Maryland, College Park, MD, USA.

Qin, H., Xu, Q., Li, W., et al., 2017. Effect of stator geometry on the emulsification and extraction in the inline single-row blade-screen high shear mixer. Ind. Eng. Chem. Res. 56 (33), 9376–9388.

Rodgers, T.L., Cooke, M., 2012. Rotor–stator devices: The role of shear and the stator. Chem. Eng. Res. Des. 90, 323–327.

Rueger, P.E., Calabrese, R.V., 2013a. Dispersion of water into oil in a rotor–stator mixer. Part 1: Drop breakup in dilute systems. Chem. Eng. Res. Des. 91, 2122–2133.

Rueger, P.E., Calabrese, R.V., 2013b. Dispersion of water into oil in a rotor–stator mixer. Part 2: effect of phase fraction. Chem. Eng. Res. Des. 91, 2134–2141.

Saarenrinne, P., Piirto, M., Eloranta, H., 2001. Experiences of turbulence measurement with PIV. Meas. Sci. Technol. 12, 1904–1910.

Sharp, K.V., Adrian, R.J., 2001. PIV study of small-scale flow structure around a Rushton turbine. AIChE Journal 47 (4), 766–778.

Sheng, J., Meng, H., Fox, R.O., 2000. A large eddy PIV method for turbulence dissipation rate estimation. Chemical Engineering Science 55, 4423–4434.

Shi, J., Xu, S., Qin, H., et al., 2013. Single-pass emulsification processes in two different inline high shear mixers. Ind. Eng. Chem. Res. 52 (40), 14463–14471.

Sparks, T. (1993) Operational characteristics of rotor/stator mixers. MPhil Thesis, Cranfield University, UK.

Sparks, T., 1996. Fluid Mixing in Rotor/Stator Mixers PhD Thesis. Cranfield University, UK.

Thapar, N., 2004. Liquid-liquid Dispersions from In-line Rotor-stator Mixers PhD Thesis. Cranfield University, UK.

Utomo, A.T., 2009. Flow Patterns and Energy Dissipation Rates in Batch Rotor-stator Mixers PhD Thesis. The University of Birmingham.

Utomo, A.T., Baker, M., Pacek, A.W., 2008. Flow pattern, periodicity and energy dissipation in a batch rotor–stator mixer. Chem. Eng. Res. Des. 86, 1397–1409.

Utomo, A.T., Baker, M., Pacek, A.W., 2009. The effect of stator geometry on the flow pattern and energy dissipation rate in a rotor–stator mixer. Chem. Eng. Res. Des. 87, 533–542.

Westerweel, J., 1997. Fundamentals of digital particle image velocimetry. Meas. Sci. Technol. 8 (12), 1379.

Westerweel, J., Elsinga, G.E., Adrian, R.J., 2013. Particle Image Velocimetry for Complex and Turbulent Flows. Annu. Rev. Fluid Mech. 45 (1), 409–436.

Xu, D., Chen, J., 2013. Accurate estimate of turbulent dissipation rate using PIV data. Exp. Therm Fluid Sci. 44, 662–672.

Xu, S., Cheng, Q., Li, W., et al., 2013a. LDA measurements and CFD simulations of an in-line high shear mixer with ultrafine teeth. AIChE Journal 60 (3), 1143–1155.

Xu, S., Shi, J., Cheng, Q., et al., 2013b. Residence time distributions of in-line high shear mixers with ultrafine teeth. Chem. Eng. Sci. 87, 111–121.

Zhang, C., Gu, J., Qin, H., et al., 2017. CFD analysis of flow pattern and power consumption for viscous fluids in in-line high shear mixers. Chem. Eng. Res. Des. 117, 190–204.

Zhang, J., Xu, S., Li, W., 2012. High shear mixers: A review of typical applications and studies on power draw, flow pattern, energy dissipation and transfer properties. Chem. Eng. Process. 57–58, 25–41.